

# 1 Climatological Statistics of Extreme Geomagnetic

## 2 Fluctuations with Periods from 1 s to 60 min

3 N. C. Rogers<sup>1</sup>, J. A. Wild<sup>1</sup>, E. F. Eastoe<sup>1</sup>, and J. Hübert<sup>2</sup>

4 <sup>1</sup>Lancaster University, Lancaster, UK

5 <sup>2</sup>British Geological Survey, Edinburgh, UK

### 6 *Abstract*

7 Using a global database of 125 magnetometers covering several decades we present occurrence statistics for  
8 fluctuations of the horizontal geomagnetic field ( $dB_h/dt$ ) exceeding the 99.97<sup>th</sup> percentile ( $P_{99.97}$ ) for both ramp  
9 changes ( $R_n$ ) and the root-mean-square ( $S_n$ ) of fluctuations over periods,  $\tau$ , from 1 to 60 min and describe their  
10 variation with geomagnetic latitude and magnetic local time (MLT). Rates of exceedance are explained by  
11 reference to the magneto-ionospheric processes dominant in different latitude and MLT sectors, including ULF  
12 waves, interplanetary shocks, auroral substorm currents, and travelling convection vortices. By fitting Generalised  
13 Pareto tail distributions above  $P_{99.97}$  we predict return levels (RLs) for  $R_n$  and  $S_n$  over return periods of between 5  
14 and 500 years.  $P_{99.97}$  and RLs increase monotonically with frequency ( $1/\tau$ ) (with a few exceptions at auroral  
15 latitudes) and this is well modelled by quadratic functions whose coefficients vary smoothly with latitude. For  
16 UK magnetometers providing 1-s cadence measurements, the analysis is extended to cover periods from 1 to  
17 60 seconds and empirical Magnetotelluric Transfer functions are used to predict percentiles and return levels of  
18 the geoelectric field over a wide frequency range ( $2 \times 10^{-4}$  to  $4 \times 10^{-2}$  Hz) assuming a sinusoidal field  
19 fluctuation. These results help identify the principal causes of field fluctuations leading to extreme  
20 geomagnetically induced currents (GIC) in ground infrastructure over a range of timescales and they inform the  
21 choice of frequency dependence to use with  $dB_h/dt$  as a GIC proxy.

### 22 *Key points*

- 23 1. Occurrence rates of extreme geomagnetic fluctuations ( $dB_h/dt$ ) are mapped against magnetic local time,  
24 latitude, and season.
- 25 2. The log frequency (or timescale) dependence of  $dB_h/dt$  is well modelled by quadratic functions  
26 parameterised by geomagnetic latitude.
- 27 3. Electric fields calculated at 3 UK sites peak at periods of 20 min at the 99.97<sup>th</sup> percentile but 0.5–2 min  
28 for 1/100-year events.  
29

30

31 *Plain language summary*

32 On rare occasions, an eruption on the sun's surface sends a cloud of energetic electrically-charged particles  
33 out into interplanetary space. When this arrives at the Earth it can cause large electrical currents to flow  
34 around the magnetic field surrounding the Earth (the 'magnetosphere') and through the upper atmosphere.  
35 These currents are detected on the ground as fluctuations in the magnetic field and may induce unwanted  
36 electrical currents in high-voltage power lines or other long metallic cables and pipelines. The rate of change  
37 of the magnetic field is used together with measurements of ground conductivity to calculate the electric field  
38 that drives such 'geomagnetically induced currents'. In this study we report the rate of occurrence of  
39 extremely rapid fluctuations in the magnetic field, and how this depends on latitude and time of day. We  
40 model the dependence of the size of the fluctuations on their timescales since this is important for estimating  
41 the subsequent response of the power grid. The patterns of extreme occurrences are explained by reference  
42 to known electrical current systems and waves in the magnetosphere and upper atmosphere, and we use  
43 statistical methods to predict the size of fluctuations expected over periods from 5 to 500 years.

## 44 1 Introduction

45

46 Large electrical currents are occasionally induced in ground-based infrastructure as a result of rare and intense  
47 currents in the ionosphere or magnetosphere. These Geomagnetically Induced Currents (GIC) have been identified  
48 as a substantial hazard to national infrastructure (Cannon et al., 2013; Hapgood et al., 2021) since they may cause  
49 catastrophic failure in high-voltage electricity supply networks (Gaunt, 2016; Oyedokun & Cilliers, 2018;  
50 Thomson et al., 2010), damage long-cable communication systems (Nevanlinna et al., 2001) and cause railway  
51 signalling errors (Boteler, 2021; Eroshenko et al., 2010; Wik et al., 2009). The cumulative effect of GICs above  
52 a certain threshold may also cause corrosion in oil and gas pipelines (Boteler, 2000; Pulkkinen et al., 2001). The  
53 science of GICs and their effects is reviewed in Knipp, 2011, Chapter 13, and Buzulukova, 2017, Chapter 8.

54 Modelling the risk of extreme GICs requires a statistical characterisation of the geoelectric field,  $\mathbf{E}$ , induced by  
55 electrical currents in the ionosphere and magnetosphere. This information may, for example, be combined with a  
56 model of electrical impedances in a high-voltage (HV) electricity network (Boteler & Pirjola, 2017) to determine  
57 the ‘return level’ (RL) of GIC expected in a ‘return period’ of 100 years or more. Direct measurements of  $\mathbf{E}$  are  
58 often subject to contamination from anthropogenic electromagnetic interference and require an experienced expert  
59 to remove noise and biases (Kelbert et al., 2017). They are also not global in extent, and do not cover the decades  
60 required for accurate prediction over long return periods. For climatological studies it is therefore expedient to  
61 instead use an archive of measurements of the rate of change of the horizontal component of the geomagnetic  
62 field,  $dB_h/dt$ , measured at ground level. Using Faraday’s law of induction (Faraday, 1832) and magneto-telluric  
63 (MT) theory (Cagniard, 1953; Chave & Jones, 2012) these may be combined with a model of the local ground  
64 conductivity to determine climatological statistics for  $\mathbf{E}$ . Alternatively,  $\mathbf{E}$  may be derived using collocated  
65 measurements of ground impedance at a magnetometer site.

66 The calculation of  $\mathbf{E}$  requires knowledge of both the temporal spectrum of geomagnetic oscillations and the  
67 frequency dependence of the surface impedance. Databases of impedance tensors are increasingly available for  
68 public use (e.g. Kelbert et al. 2011; Kelbert et al. 2018) and can cover a wide frequency range corresponding to  
69 periods from milliseconds to hours. The most effective source of geoelectric fields producing damaging GIC in  
70 power transmission lines lie in 1–1000 s period oscillations (Kappenman, 2004; Barnes et al., 1991) and electricity  
71 companies have identified that fluctuations on timescales from tens of seconds to over an hour have led to  
72 vulnerability of high-voltage (HV) electricity networks to GIC (e.g., NERC, 2017; Girgis & Vedante, 2012). A  
73 well-reported example is the geomagnetic storm of 13 March 1989 in which the 21 GW Hydro-Québec power  
74 supply failed for nine hours following horizontal geomagnetic field fluctuations  $|dB_h/dt|$  of approximately  
75 500 nT/minute (p.640, Knipp, 2011).

76 The frequency of the induced  $\mathbf{E}$  field fluctuations and consequent GICs is much less than the frequency of high-  
77 voltage electricity networks (50 or 60 Hz) and so is often modelled as a quasi-direct current. Currents of more  
78 than a few amperes sustained over periods similar to the thermal time constants of the components of a high-  
79 voltage transformer – typically 30–45 minutes – may cause irreversible damage resulting in power failures (p.8,  
80 IEEE, 2015; Girgis & Vedante, 2012; Erinmez et al., 2002; Molinski, 2002; NERC, 2017). GICs generated by  
81 field fluctuations with periods longer than 1 hour have amplitudes too small to be of concern, whilst sub- 1-s

82 fluctuations are heavily damped by inductances in electric power systems (Boteler & Pirjola, 2017).  
83 Understanding the climatology of extreme  $|dB_h/dt|$  over periods from 1 s to 1 hour should, therefore, help to  
84 quantify the GIC risk to electrical power systems.

85 Large-scale statistical surveys often exploit measurements at 1-min resolution, in large part enabled by the  
86 successful SuperMAG project (Gjerloev, 2011), thus many have examined only the 1-minute changes in  $B_h$ ,  
87 (denoted  $R_I$ ), with this metric being adopted as a proxy for GICs (e.g. Viljanen et al., 2001, 2015; Thomson et al.,  
88 2011). However, probability distributions of  $|dB_h/dt|$  are observed to depend strongly on the time resolution (or  
89 sample averaging period) of the  $B$  field measurements, with lower amplitudes at longer sampling intervals due to  
90 the effect of smoothing. In recent years, an increasing number of magnetometer operators have offered users  
91 measurements at 1-s cadence and so the question arises as to which temporal resolution to apply when using  
92  $|dB_h/dt|$  as a proxy indicator for GIC. Modelling by (Pulkkinen et al., 2006) showed that smoothing the  $B$ -field  
93 components from their native resolution of 1 s up to 60 s reduced the amplitude of  $|dB_h/dt|$  by 80% whilst the  
94 computed peak E-field amplitudes were reduced by only 20%, the inference being that a 60-s (but no more) sample  
95 interval is acceptable as a proxy to use for  $E$ -field (and hence GIC) calculations. Other studies have noted that  
96 rather than taking  $R_I$  as a proxy for GIC, a better performing indicator was obtained by taking an average  $dB_h/dt$   
97 over 20-minutes (Tóth et al., 2014) or 30 minutes (Viljanen et al., 2015), whilst others have used the hourly range  
98 or standard deviation (Beamish et al. 2002; Nikitina et al., 2016; Danskin & Lotz, 2015) or 3-hourly range indices  
99 as a proxy (Trichtchenko & Boteler, 2004).

100

101 In several cases, the magnitude of  $B_h$  relative to its quiet-day value (often denoted  $\Delta H$ ) has provided a better proxy  
102 for GIC than  $dB_h/dt$  (Pulkkinen et al., 2010; Tóth et al., 2014; Watari et al., 2009). Pirjola (2010) showed  
103 how this is more likely to arise in regions for which there is an upper, highly conductive layer overlying a deeper  
104 layer of low conductivity. Heyns et al. (2020) presented examples of GIC amplitudes and phases matching closely  
105 to the 20-min period fluctuations of the field ( $\Delta H$ ) which were poorly represented by high-cadence  $dB_h/dt$   
106 indicators, whilst  $dB_h/dt$  was a better indicator of the rapid field variation that occurred during Sudden  
107 Commencements, which often initiate geomagnetic storms. Heyns et al. (2020) explained that this is because the  
108  $B$  field (or  $\Delta H$ ) has low-frequency components that are deweighted when taking the time derivative – for example,  
109 if  $B_h = B_0 \exp(i\omega t)$  then frequency components of  $|dB_h/dt|$  are weighted by the factor  $1/\omega$ . Consequently, 1-s  
110 resolution  $dB_h/dt$  measurements ( $R_{1/60}$ ) would be even less effective as a proxy for GIC (compared to  $R_I$ ) for  
111 GIC caused by field fluctuations of a much longer period. Power networks can respond strongly to  $B$ -field  
112 fluctuations over tens of minutes, indicative of finite reactive impedances in the network components, and  
113 assumptions that the geomagnetic driving is d.c. in nature may be insufficient to replicate the observed GIC (Heyns  
114 et al., 2020; Jankee et al., 2020).

115

116 The study of extreme geomagnetic fluctuations over a range of periods yields much information about the causes  
117 and impacts of GIC as well as the drivers of these fluctuations. The ionospheric and magnetospheric processes  
118 contributing to  $dB_h/dt$  over a 1-min period will differ greatly from those at 60 min and will depend on the latitude,  
119 magnetic local time (MLT), season, and other factors. The principal drivers of short transients (timescales of  
120 minutes) may be categorised into the following phenomena:

121

122

123

124

125

126

127

128

129

130

131

132

133

134

135

136

137

138

139

140

141

142

143

144

145

146

147

148

149

150

151

152

153

154

155

156

157

158

159

160

1. **Sudden Commencements (SC):** Interplanetary shocks arriving in the solar wind, which generate a sudden eastward (dusk-to-dawn) Chapman-Ferraro current at the dayside magnetopause, are observed as Sudden Commencements (SC) in magnetograms (Fiori et al., 2014; Kappenman, 2003; Smith et al., 2019). The characteristic rapid magnetic field variation may be short-lived, lasting several minutes or up to an hour (Knipp, 2011, p.496), and are associated with  $dB_h/dt$  of up to 30 nT/min at low geomagnetic latitudes ( $< 40^\circ$ ) or up to a maximum of 270 nT/min in the auroral zone (approximately  $65^\circ$  geomagnetic latitude) (Fiori et al., 2014).
2. **Auroral substorm onsets:** A substorm is the sudden brightening and expansion of auroral arcs resulting from bursts of energetic electron precipitation from the magnetotail (Akasofu, 2017; Ieda et al., 2018). This enhances the ionisation and electrical conductivity of the ionospheric  $E$  region allowing strong Hall currents to flow, most often in a westward direction which manifest in magnetograms as a rapid decline in the north component of the geomagnetic field,  $B_N$ . Substorm onsets have been categorised by Newell & Gjerloev (2011) from the SML geomagnetic index (which measures the lower envelope of  $B_N$ ) as a reduction of at least 45 nT over 3 minutes followed by a mean level at least 100 nT below the initial value during the half-hour following onset.
3. **Day-time Magnetic Impulse Events (MIE):** Pairs of up- and down- field aligned currents generated by a pulse in dynamic pressure at the dayside magnetopause couple into the ionosphere as Travelling Convection Vortices (TCV) at latitudes in the vicinity of the dayside cusp/cleft (approximately  $77-78^\circ$  magnetic) (Zesta et al., 2002; Kataoka, 2003; Engebretson et al., 2013; Friis-Christensen et al., 1988; Lanzerotti et al., 1991). Magnetometers in this region observe the ionospheric Hall current loops (a pair of vortices) as isolated magnetic impulse events (MIE) in magnetograms, lasting typically 5-15 minutes with amplitudes of typically 50–200 nT or up to a maximum of 400 nT (Kataoka et al., 2003; Lanzerotti et al., 1991). Several mechanisms have been postulated to explain the generation of TCVs near the dayside magnetopause, including bursts of magnetic field line reconnection (flux transfer events), solar wind pressure pulses, plasma injections into the low-latitude boundary layer, Kelvin-Helmholtz instabilities, and perturbations of the ion foreshock upstream of the Earth's bow shock (see references in Kataoka et al., 2003 and Engebretson et al., 2013). In general, TCVs are defined so as to exclude sudden commencement perturbations associated with a large interplanetary shock (e.g. Pilipenko et al., 2019).
4. **Night-time Magnetic Perturbation Events (MPE):** MPEs are a broad class of large (hundreds of nT), localised, 5-10 min unipolar or bipolar pulses of  $B_h$  which occur in the auroral zone during substorms, but are not necessarily associated with substorm onsets (Engebretson et al., 2019a,b, 2020, 2021; Belakhovsky et al., 2019; Dimmock et al., 2019; Apatenkov et al., 2020; Viljanen, 1997). They arise from transient phenomena in the magnetotail such as bursty bulk flows (BBFs) (Angelopoulos et al., 1992; Wei et al., 2021), dipolarising flux bundles (Liu et al., 2014), poleward-expanding discrete aurorae passing over the magnetometer site (Ngwira et al., 2018), and small-scale rapidly moving ionospheric current vortices (Apatenkov et al., 2020).

A significant number of GIC events occur under geomagnetic storm conditions at auroral and mid-latitudes due to sustained ULF pulsations in the Pc5 band (2.5–10 min period field oscillations (Baker et al., 2003; McPherron,

161 2005; Pilipenko et al., 2010; Ziesolleck & McDiarmid, 1995)). These may be driven by Alfvén wave Kelvin-  
 162 Helmholtz instabilities in the magnetosphere and are often initiated by the arrival of a shock in the solar wind or  
 163 a high-speed solar wind stream (>500 km/s) (Engebretson et al., 1998; Pahud et al., 2009; Vennerstrøm, 1999;  
 164 Zhang et al., 2010; Hao et al., 2019). In addition, auroral omega bands (Apatenkov et al., 2020; Belakhovsky et  
 165 al., 2019) may manifest in magnetograms as quasi-periodic (4-40 min) “Pi3” or “Ps6” geomagnetic fluctuations  
 166 on the morning side during the recovery phases of substorms (Jorgensen et al., 1999; Saito, 1978; Wild et al.,  
 167 2000) or during substorm expansions in the midnight sector (Wild et al., 2011).

168

169 *B*-field fluctuations over tens of minutes may also arise from the expansion and recovery phases of substorms in  
 170 the auroral zone (Freeman et al., 2019; Pothier et al., 2015): The substorm expansion phase typically lasts 25–40  
 171 minutes (Pothier et al., 2015) followed by a more gradual recovery phase. Changes over an hour or more may  
 172 arise from slow changes and movements of an electrojet over a magnetometer station or from gradual changes of  
 173 the magnetospheric inner ring current intensity during the main and recovery phases of a geomagnetic storm.

174

175 At very high latitudes (poleward of the dayside cusp) and under conditions of northward interplanetary magnetic  
 176 field (IMF) and large dipole tilt (e.g. at summer noon), magnetic fluctuations may be associated with the merging  
 177 of ‘overdraped’ tail-lobe field lines with the IMF (Crooker, 1992; Watanabe et al. 2005). Rogers et al. (2020)  
 178 postulated that field-line reconnections may drive impulsive ‘Region-0’ field-aligned currents (Wang et al. 2008;  
 179 Milan et al. 2017) into this region that could manifest as large  $|dB_h/dt|$  fluctuations at the surface.

180

181 In this paper we have extended a global climatological statistical model of extreme 1-minute fluctuations,  $R_1$ ,  
 182 (Rogers et al., 2020) to include the magnitude and frequency of occurrence of extreme  $|dB_h/dt|$  over sampling  
 183 periods between 1 and 60 minutes, both as ramp changes (applying a moving average of the geomagnetic field  
 184 measurements) and as a root-mean-square (RMS) of the  $R_1$  values over  $n$ -minute periods that we denote  $S_n$  for  
 185  $n = 1-60$  (defined explicitly in Section 2). The latter is a measure of the sustained power in extreme geomagnetic  
 186 field fluctuations, which is important in modelling the risk to transformer components due to heating, for example.  
 187 Our study complements that of Love et al. (2016a) who provided an analysis of extreme  $|dB_h/dt|$  over 1- and  
 188 10-minute periods, ( $R_1$  and  $R_{10}$ ), and the RMS of  $R_1$  over 10 minutes ( $S_{10}$ ). Wintoft (2005) and Wintoft et al. (2005)  
 189 also chose to study  $S_{10}$  as a predictor of the RMS GIC amplitude. Part of our study will focus on three UK  
 190 magnetometer sites, and as such complements the work of Beamish et al. (2002) – who examined the hourly  
 191 standard deviation of 1-min *B*-field north and east components (independently), a measure similar to the  $S_{60}$   
 192 calculated in this paper – and the works of Beggan et al. (2013) and Beggan (2015), who estimated extreme *E*-  
 193 field and GICs for the UK national grid at 100- and 200-year return periods using UK ground conductivity models  
 194 for 2 and 10-min period fluctuations of the inducing *B*-field, with amplitudes inferred from predicted extremes of  
 195  $R_1$  presented by Thomson et al., (2011).

196

197 In section 2 we describe the processing of magnetometer measurements data set and the determination of extreme  
 198 values for  $|dB_h/dt|$  as both ramp changes and RMS fluctuations. Section 3 presents the latitude and MLT  
 199 distributions of large percentiles and projected extreme values for a range of sampling frequencies and develops

200 a global model to characterise the dependences on sampling frequency. The frequency range is extended up to  
 201 1 Hz sampling for three UK sites, and for these locations empirical MT transfer functions (or surface impedance  
 202 matrices) are used to predict high percentiles and extreme values of the geoelectric field.

## 203 2 Measurements

204 Magnetic field measurements (magnetograms) were obtained from 125 magnetometers in the global SuperMAG  
 205 collaboration (Gjerloev, 2011) at sites for which at least 20 years of data was available, with an average of 28  
 206 years' data per site. Table 1 provides the locations of these magnetometer sites in geodetic and corrected  
 207 geomagnetic (CG) coordinates (Laundal & Richmond, 2017; Shepherd, 2014). Due to the secular variation of the  
 208 Earth's main field, CG coordinates are given as averages over all years in which magnetometer data was available  
 209 at each site. In this paper we consider only the north and east components of the magnetic field ( $B_N$  and  $B_E$ ,  
 210 respectively) in local magnetic coordinates (Gjerloev, 2012) neglecting the downward vertical field component,  
 211  $B_z$ , which contributes little to GICs in surface-based infrastructure. The magnetograms provided by SuperMAG  
 212 had already been cleaned and manually inspected to remove most artificial sudden changes in the baseline  
 213 (offsets), spikes, and gradual slopes (Gjerloev, 2012). Nonetheless, as a further check, all data in weeks containing  
 214  $R_I$  peaks above the 99.97<sup>th</sup> percentile ( $P_{99.97}$ ) were visually inspected and obvious artefacts (such as large spikes,  
 215 step changes, and instrument saturation effects) were replaced by data gaps, as described in (Rogers et al., 2020).

216 At each magnetometer, the 'ramp' change in the horizontal component of  $\mathbf{B}$  over  $n$ -minute intervals was defined  
 217 as

$$\mathbf{R}_n = \{R_n(i): i = 1, 2, 3, \dots, k\} \quad (1)$$

$$R_n(i) = \sqrt{\left(\frac{B_N(i) - B_N(i-n)}{n\Delta t}\right)^2 + \left(\frac{B_E(i) - B_E(i-n)}{n\Delta t}\right)^2} \quad (2)$$

218 where  $k$  is the number of field measurements, and  $\Delta t = 1$  minute was the cadence of the measurements. For  
 219 computational efficiency, the  $n$ -minute backward difference values,  $\mathbf{R}_n$ , were calculated using  $n$ -point moving-  
 220 average filters on the 1-minute first differences of  $B_N$  and  $B_E$ . Intervals containing missing data were excluded  
 221 from the analysis. The statistics of  $\mathbf{R}_1$  (1-min field fluctuations) were modelled in (Rogers et al., 2020). The  
 222 definition in (2) ensures that statistics of the induced E-field magnitude,  $|E| = \sqrt{E_N^2 + E_E^2}$  will be approximately  
 223 proportional to  $R_n$  (with exact proportionality for an idealised half-space model of surface conductivity – see  
 224 Annex A). The expression for  $R_1$  is the same as that adopted by Freeman et al. (2019), Smith et al. (2019), Wintoft  
 225 et al. (2015, 2016), Ngwira et al. (2018), Falayi et al. (2017), Kozyreva et al. (2018) and others, but differs slightly  
 226 from the first differences of  $B_h$  (i.e.  $d|B_h|/dt$ ) computed by some authors (e.g. Love et al., 2016a; Thompson et  
 227 al., 2011) particularly when there is a rapid change in field direction.

228 The root-mean-square of  $\mathbf{R}_1$  over  $n$ -minute periods was defined as

$$\mathbf{S}_n = \{S_n(i), \quad i = 1, 2, 3, \dots, k\} \quad (3)$$

229 with

$$S_n(i) = \sqrt{\frac{1}{n} \sum_{j=i-n+1}^i R_1(j)^2} \quad (4)$$

230 and this was implemented in software using a convolution filter. Since we are only interested in extreme values,  
 231 a high threshold for  $R_n$  and  $S_n$  was set at the 99.97<sup>th</sup> percentile level,  $P_{99.97}$ . The application of extreme value  
 232 statistics (Coles, 2001) requires an assumption that exceedances of this threshold are temporally independent  
 233 rather than clustered together. Therefore, the threshold exceedances were declustered to ensure a minimum  
 234 12 hours between clusters and only the peak value in each cluster was recorded. The magnetic local times (MLT)  
 235 (Laundal & Richmond, 2017) associated with each peak were also calculated as described by Rogers et al. (2020).  
 236 Declustered exceedances ( $R_n > P_{99.97}$ ) were then fitted to a Generalised Pareto (GP) ‘tail’ distribution and the  
 237 fitted GP profile was used to predict return levels (RL) expected over return periods (RP) of up to 500 years (see  
 238 (Rogers et al., 2020) and (Coles, 2001) for mathematical details). The analysis of extreme field fluctuations at 28  
 239 European magnetometer sites by Thomson et al. (2011) showed that the choice of a  $P_{99.97}$  threshold and 12-hour  
 240 declustering provides relatively stable GP coefficients whilst ensuring temporal independence of the extreme  
 241 events. For consistency of approach we have therefore adopted these thresholds for our analysis of magnetometer  
 242 data worldwide.

243 A further set of magnetometer measurements at 1-s cadence were obtained for three sites in the UK operated by  
 244 the British Geological Survey, namely, HAD (Hartland, southern England, CG latitude  $\lambda = 47.55^\circ$ ), ESK  
 245 (Eskdalemuir, southern Scotland,  $\lambda = 52.65^\circ$ ), and LER (Lerwick, Shetland Is, northern Scotland,  $\lambda = 57.97^\circ$ ) (see  
 246 Table 1). Data at 1-s resolution were available from 1 Jan 2001 to 14 Sep 2016 for all three sites, whilst the 1-min  
 247 SuperMAG data set extended from 1 January 1983 to 31 December 2016 for all three sites. The data were visually  
 248 inspected for weeks containing 1-s  $|dB_h/dt|$  ( $R_{1/60}$ ) exceeding the 99.97<sup>th</sup> percentile, and obvious artefacts  
 249 removed in the same manner as for the 1-minute SuperMAG data set described above. When fitting GP  
 250 distributions to predict return levels for the 1-s datasets, and for all averaging periods,  $\tau \equiv n \Delta t$ , we have used the  
 251 same consistent percentile threshold (99.97<sup>th</sup> percentile) and declustering run-length (12-h) as selected in the study  
 252 of 1-min cadence measurements by Thomson et al. 2011 using a selection of visual diagnostics. Thomson et al.  
 253 (2011) noted that, for most geomagnetic observatories in their study, the return level was “only weakly dependent  
 254 on the decluster length”. Historically, in extreme value statistical analyses, justification of the threshold selected  
 255 has been through visual diagnostics combined with any available scientific insight or expert knowledge on the  
 256 process of interest. The use of visual diagnostics becomes infeasible as the number of data sets (in this case site-  
 257 frequency combinations) grows. Consequently, we took a pragmatic approach and defined the same proportion of  
 258 observations to be the tail sample for each site and for each value of  $\tau$ . For a given  $\tau$ , this permits comparison of  
 259 return levels across sites, and for a given site it permits comparison across all values of  $\tau$ . As the duration of the  
 260 1-s datasets obtained from the UK observatory sites differed from those in the 1-min data set in the SuperMAG  
 261 archive, we ran additional visual diagnostic checks for thresholds at 99.95, 99.97 and 99.99 percentiles (with and  
 262 without 12-h declustering applied) as were performed in the analysis by Thomson et al. (2011). These checks  
 263 confirmed that for the  $\Delta t = 1$  s dataset, 12-h declustering and the 99.97<sup>th</sup> percentile threshold remained the most  
 264 appropriate for return level estimation at all three UK observatories.

265 The measurement of the ground magnetic field has a long established tradition in many countries and data quality  
 266 and standards are set to a high level, e.g. through INTERMAGNET (Thomson & Flower, 2021; Love & Chulliat,  
 267 2013). In contrast, long-term observations of the ground electric field are relatively rare (Beggan et al., 2021 and  
 268 references therein) and more influenced by man-made electromagnetic noise due to a low signal-noise ratio.  
 269 Available data sets are scarce and often discontinuous. In the UK, the ground electric field has been monitored at  
 270 the three geomagnetic observatories (HAD, ESK, and LER) since 2015 with non-polarizable electrodes along  
 271 north-south (N-S) and east-west (E-W) oriented baselines. (Some recent examples of these measurements are  
 272 available online: [http://www.geomag.bgs.ac.uk/data\\_service/space\\_weather/geoelectric.html](http://www.geomag.bgs.ac.uk/data_service/space_weather/geoelectric.html).)

273 To obtain estimates of the geoelectric field for times when no data was recorded, the horizontal geoelectric field  
 274 spectrum,  $\mathbf{E}(f) = \begin{pmatrix} E_x \\ E_y \end{pmatrix}$  may be estimated from the horizontal magnetic field spectrum  $\mathbf{B}(f) = \begin{pmatrix} B_x \\ B_y \end{pmatrix}$  via

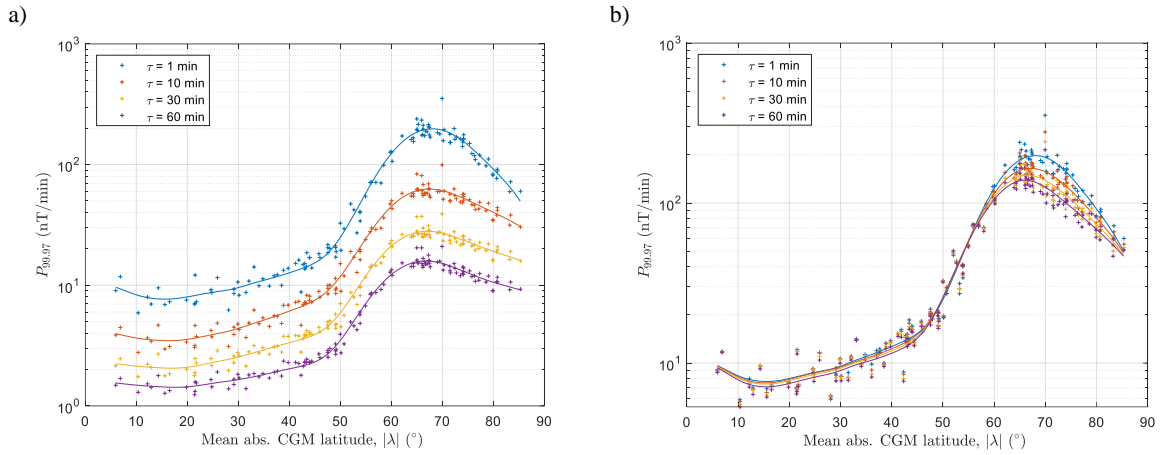
$$\mathbf{E}(f) = \mathbf{Z}(f)\mathbf{B}(f)/\mu \quad (5)$$

275 where  $\mu$  is the permeability, and  $\mathbf{Z}(f) = \begin{pmatrix} Z_{xx} & Z_{xy} \\ Z_{yx} & Z_{yy} \end{pmatrix}$  is the impedance (with units of  $\Omega$ ), where  $x$  and  $y$  refer to  
 276 north and east components, respectively (e.g., Chave & Jones, 2012, Simpson & Bahr, 2005). Fourier transforms  
 277 may be used to convert between the frequency ( $f$ ) and time domains. The frequency-dependent term  $\mathbf{Z}/\mu$  is called  
 278 the Magnetotelluric (MT) transfer function (with units of V/km/nT) and is informative of the electrical  
 279 conductivity structure of the subsurface that is useful in deep geophysical exploration.

280  $\mathbf{Z}/\mu$  was estimated from simultaneous measurements of the horizontal components of the ground electric and  
 281 magnetic field using robust statistical approaches to minimize the influence of noise. For the estimation of  $\mathbf{Z}/\mu$  at  
 282 HAD, ESK and LER, we used six months of electric and magnetic field measurements from 2015 and applied the  
 283 impedance estimation algorithm of Smirnov (2003). Further details of the procedure are given in (Beggan et al.,  
 284 2021). Due to the sampling cadence of 1 s and the frequency response of the fluxgate magnetometers at the  
 285 observatory sites, the impedance estimates cover a period range of 20 to 20,000 s (or  $5 \times 10^{-2} - 5 \times 10^{-5}$  Hz).

### 286 3 Latitude, MLT, and Seasonal distribution of large $R_n$ and $S_n$ on 287 timescales from 1 to 60 min

288 Figure 1 presents the 99.97<sup>th</sup> percentiles of a) Ramp changes ( $R_n$ ) and b) RMS fluctuations ( $S_n$ ) at four sampling  
 289 intervals,  $\tau \equiv n \Delta t = 1, 10, 30,$  and 60 min, plotted against the mean absolute CG latitude,  $|\lambda|$ . Each point in the  
 290 graphs represents  $P_{99.97}$  at an individual magnetometer site, and the solid curves are smoothed spline fits to the  
 291 data.



292 Figure 1. 99.97<sup>th</sup> percentiles of a) ramp changes ( $R_1$ ,  $R_{10}$ ,  $R_{30}$ , and  $R_{60}$ ) and b) RMS variations ( $S_1$ ,  $S_{10}$ ,  $S_{30}$ , and  $S_{60}$ ). Solid lines  
 293 are smoothed spline fits.

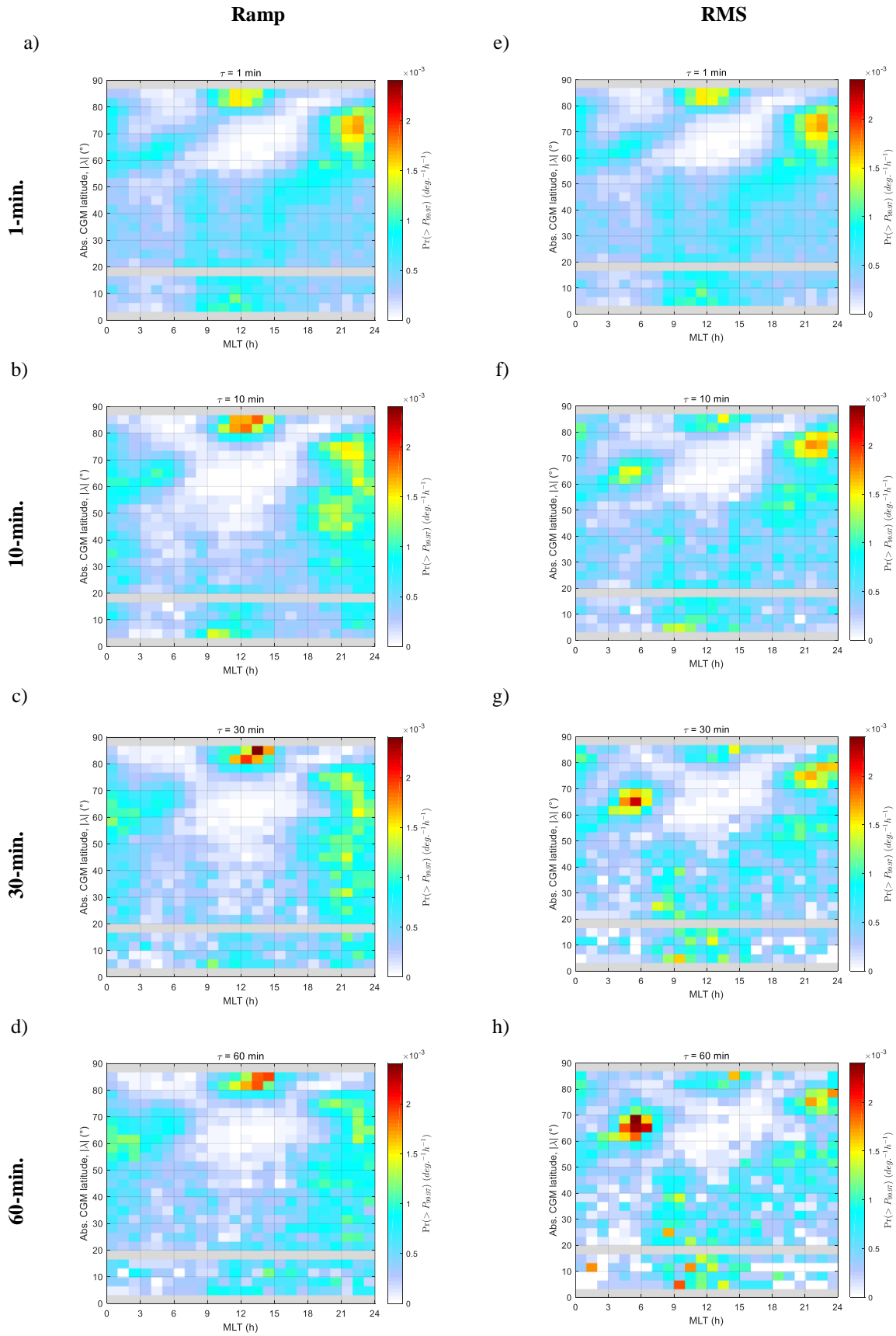
294 The shapes of the profiles  $P_{99.97}(|\lambda|)$  are broadly similar for both  $R_n$  and  $S_n$  and for all  $\tau$ , consisting of a broad  
 295 maximum centred about  $|\lambda| \cong 67^\circ$ , indicative of intense auroral current systems in this region, tapering to a  
 296 minimum at  $|\lambda| \cong 15^\circ$  with a slight increase towards the equator. The latter is indicative of stronger disturbances  
 297 near the equatorial electrojets, a narrow band of enhanced ionospheric  $E$ -layer currents in the region  $|\lambda| < 5^\circ$ ,  
 298 which have previously been associated with elevated  $|dB_n/dt|$  and GIC magnitudes (Adebesin et al., 2016;  
 299 Pulkkinen et al., 2012; Carter et al., 2015; Ngwira et al., 2013). For ramp changes (Figure 1a) there is a strong  
 300 dependence on  $\tau$  and the shape of  $P_{99.97}(|\lambda|)$  changes with  $\tau$  (most clearly evident when comparing the curves for  
 301  $\tau = 1$  and 10 min). The dependence of the RMS magnitude on  $\tau$  (Figure 1b) is, to a first approximation, flat except  
 302 at latitudes above  $|\lambda| \cong 60^\circ$  where  $P_{99.97}$  decreases with increasing  $\tau$ . In Section 4 we shall further develop models  
 303 of  $P_{99.97}(|\lambda|, \tau)$  for both  $R_n$  and  $S_n$ , and present similar models for their 100-year return levels.

304 To gain a better understanding of the physical drivers of these large fluctuations, we first examine their magnetic  
 305 local time (MLT) dependence. Figure 2 presents the probability of (declustered) peaks of  $|dB_n/dt|$  exceeding  
 306  $P_{99.97}$  as a function of  $|\lambda|$  and MLT. This was calculated by counting the number of peaks in 1-hour bins of MLT  
 307 and  $3.3^\circ$  bins of  $|\lambda|$ , where data from multiple magnetometers were aggregated where they lay within the same  
 308 latitude bin. (Bin sizes were chosen as a compromise between resolution and quantisation noise.) The bin counts  
 309 were then normalised by the total number of field measurements in each bin. Panels (a–d) present the distributions  
 310 for ramp changes over 1, 10, 30 and 60 min, respectively, whilst panels (e–h) present the distributions for the  
 311 RMS magnitudes over 1, 10, 30 and 60 min, respectively. We have used absolute latitude on the vertical axes  
 312 since the distributions of occurrence probability against (signed  $\lambda$ , MLT) were, to a close approximation,  
 313 symmetric about  $\lambda = 0$ . Note that panels a) and e) are identical, which may be noted from Equation (4) with  $n=1$ .  
 314 When interpreting the distributions in Figure 2 it is important to remember that the threshold  $P_{99.97}$  itself varies  
 315 with  $|\lambda|$  (see Figure 1) and as such it is simplest to focus on the MLT distribution in each individual latitude band.  
 316 It is also important to note that, due to the method of declustering, peaks occurring within 12-hours of a larger  
 317 peak are not represented. However, it was observed that if the peaks over threshold were not declustered, then the  
 318 general shape and form of the probability distribution in Figure 2 remained largely unaltered; for  $|\lambda| > 40^\circ$ , with  
 319 no declustering, the occurrence probabilities were slightly reduced in the hours 12–24 MLT and slightly raised in  
 320 the hours 0–12 MLT, indicating a greater clustering of peaks associated with events occurring pre-noon.

321 At the highest latitudes ( $|\lambda| > 80^\circ$ ), poleward of the dayside cusp, there is an occurrence maximum in the few  
322 hours about noon MLT, which persists over all timescales (1–60 min). For  $\tau > 1$  min, the maximum is much more  
323 sharply peaked for ramp changes than for RMS fluctuations, and as  $\tau$  increases towards 60 min the MLT of the  
324 maximum occurs slightly later (towards 14 MLT). (Note that the timestamps and MLTs associated with each  
325 cluster peak of  $|dB_n/dt|$  refers to the *end* of the  $n$ -minute period in question (from Equations (2) and (4)) but this  
326 is not sufficient to account for the apparent shift of the maximum towards the post-noon.) Analysis of the  $R_I$   
327 distribution by Rogers et al. (2020) showed that these peaks near noon occur predominantly under northward IMF  
328 conditions during the summer months (i.e. under conditions of greatest dipole tilt angle), suggesting a possible  
329 relation to impulsive field line reconnection between the IMF and an ‘overdraped’ tail lobe (Wang et al., 2008;  
330 Milan et al., 2017; 2020; Crooker, 1992; Watanabe et al., 2005). The MLT distribution of occurrence probability  
331 at dayside cusp latitudes does not match the distributions of MIEs observed by Lanzerotti et al. (1991) and Kataoka  
332 et al. (2003) who reported a relatively flat distribution over 06–18 MLT with a minimum around 11 MLT, although  
333 these MIE distributions were not thresholded at a very high percentile. Nonetheless, the MIE amplitude  
334 distribution presented in Fig. 5d of (Kataoka et al., 2003) indicates perturbations approaching 400 nT (over ~5-  
335 15 min) in the 07–11 MLT period, which is not observed in the MLT profile of  $P_{99,97}$  exceedances of Figure 2a.  
336 Such discrepancies indicate that it is less likely that MIEs (caused by TCVs) provide a significant contribution to  
337 the extremes of  $|dB_n/dt|$  in this region.

338

339 At low latitudes  $|\lambda| < 40^\circ$ , for  $R_I$  and  $R_{10}$ , and  $S_n$  for all  $n$ , the occurrence probabilities increase on the day-side at  
340 07-16 MLT, although for  $20^\circ < |\lambda| < 43^\circ$  the distribution is double-peaked with a dip in occurrence in the few  
341 hours around noon, creating a Y-shaped pattern most clearly discernible in the 1-min data (panels (a) or (e)). The  
342 distributions for  $R_{10}$  and  $R_{30}$  also have a night-time maximum in the period (19-03 MLT). Rogers et al. (2020)  
343 showed (in their Fig. 8) that approximately 25-70% of the  $R_I$  peaks at these latitudes occurred at or within 30  
344 minutes of a sudden commencement, as recorded with high confidence in IAGA bulletins  
345 (<http://www.obsebre.es/en/rapid>). However, the lower figure (25%) was associated with the largest occurrence  
346 probabilities near noon, suggesting that alternative or delayed driving processes may be contributing to the largest  
347  $R_I$  at these times.



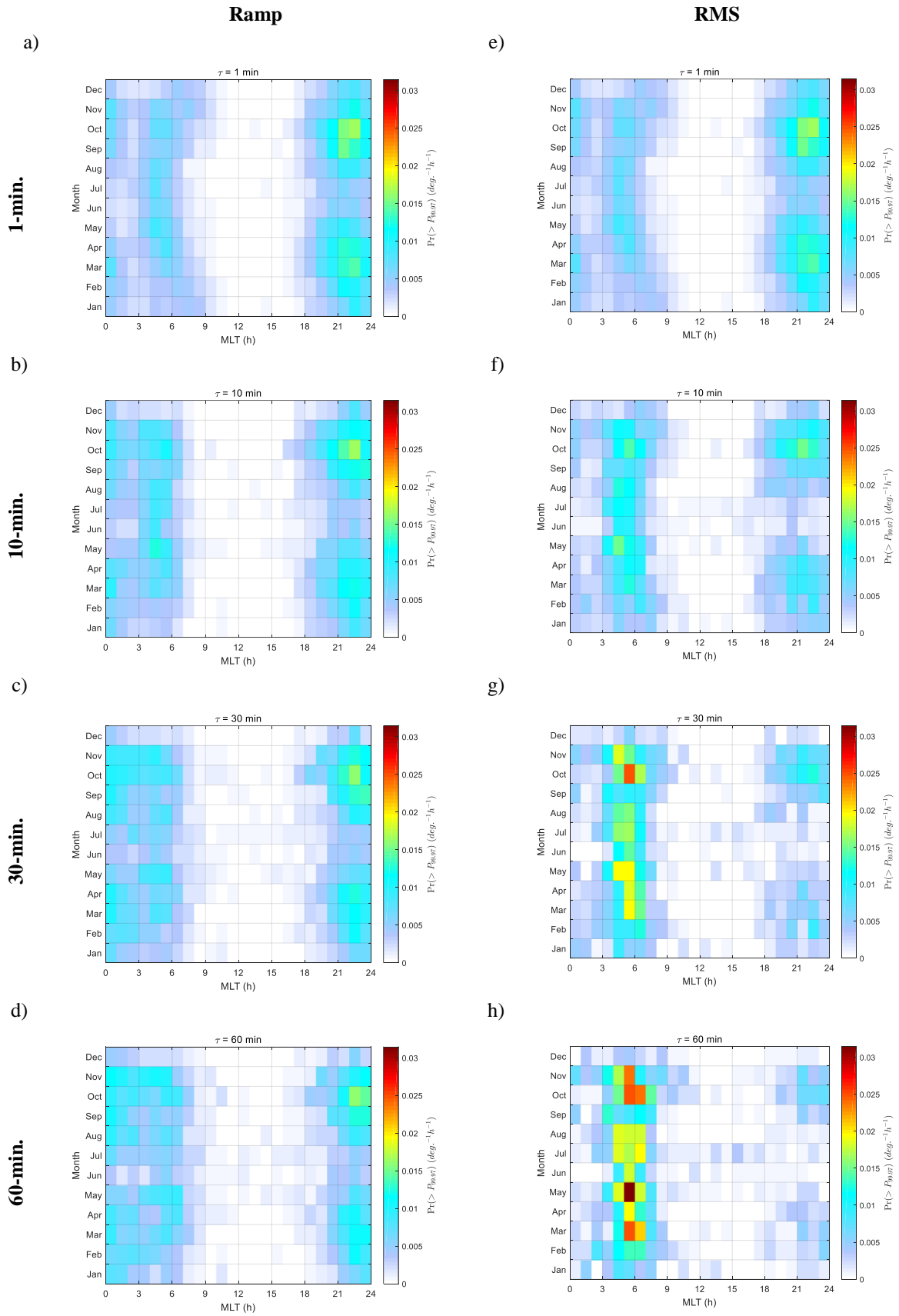
348 Figure 2.  $\Pr(|dB_h/dt| > P_{99.97})$  against CG latitude and MLT for (a)  $R_1$ , (b)  $R_{10}$ , (c)  $R_{30}$ , (d)  $R_{60}$ , (e)  $S_1(=$   
 349  $R_1)$ , (f)  $S_{10}$ , (g)  $S_{30}$ , (h)  $S_{60}$ . Latitude bins with no magnetometers are coloured grey.

350 At auroral latitudes ( $60^\circ < |\lambda| < 75^\circ$ ) the occurrence probability  $Pr(R_n > P_{99,97})$ , is greatest in the few hours before  
 351 local midnight (20–24 MLT) for all timescales. Substorm onsets occur most frequently in this MLT sector (Liou  
 352 et al., 2001; Wang et al., 2005) so the increased prevalence of large  $R_n$  may be associated with the substorm  
 353 expansion and recovery phases themselves, or with transient and localised MPEs, most of which occur within  
 354 30 min of a substorm onset. Engebretson et al. (2021) recently presented a statistical survey of MPEs at five  
 355 Canadian sites (65–75°N geomagnetic) and their Fig. 4 showed that the distributions of MPE above a threshold  
 356 of 6 nT/s (360 nT/min) (with a maximum of 37 nT/s (2220 nT/min)) contained a distribution in the range 02–06  
 357 MLT at only the lowest latitude station (65°N) whilst for the other four stations (71°N–75°N) a broad distribution  
 358 of MPE occurrence was observed in the pre-midnight hours over 19–01 MLT. This observation is consistent with  
 359 the MLT occurrence distributions shown in Figure 2a and b. The MLT of peak occurrence (in the pre-midnight  
 360 hours) is approximately one hour earlier at the mid-latitudes associated with UK magnetometers (HAD, ESK and  
 361 LER) ( $\lambda = 47.5^\circ\text{N}–58^\circ\text{N}$ ). Freeman et al. (2019) observed that, for the same three UK sites, approximately 55%  
 362 of  $R_I$  peaks exceeding  $P_{99,97}$  were associated with the expansion or recovery phase of a substorm.

363

364 A secondary peak of occurrence is observed in the dawn-noon sector. Some of these peaks below 70°N may be  
 365 associated with MPEs since they are consistent with the 02–06 MLT distribution observed by Engebretson et al.  
 366 (2021) for the station at 65°N geomagnetic, as noted above. However, this is also a region in which Pc5 pulsations  
 367 are the dominant wave activity (e.g. Engebretson et al., 1998; Pulkkinen & Kataoka, 2006). The  $R_I$  occurrence  
 368 probabilities maximise at around 03 MLT at  $|\lambda|=60^\circ$ , increasing to 12 MLT at  $|\lambda|=80^\circ$ , and similar patterns have  
 369 been reported in the distribution of Pc5 wave power (compare, for example, Fig. 5 of Vennerstrøm (1999), Fig. 2  
 370 and 4b of Baker et al., 2003, or Fig. 1 of Weigel et al., 2002). The rate of occurrence for longer-period ramp  
 371 changes,  $R_{10}$ ,  $R_{30}$  and  $R_{60}$ , is suppressed in the latitude band  $|\lambda|=70–77^\circ$ , although this may be an effect of  
 372 declustering where the peaks occur within 12 hours of larger amplitude fluctuations in the pre-midnight sector.

373 In contrast to the distribution of ramp changes, the occurrence patterns of large RMS fluctuations (Figure 2e–h)  
 374 show that as the period,  $\tau$  increases, the probability of occurrence  $Pr(S_n > P_{99,97})$  in the auroral zone increases  
 375 strongly in the dawn sector (03–07 MLT). A cursory inspection of magnetograms for the largest peaks of  $S_n$   
 376 indicated that many are indeed associated with ULF wave activity lasting tens of minutes (see, for example, Fig.  
 377 1c of (Rogers et al., 2020). To examine this further, an analysis of the probability of occurrence *vs* (month, MLT)  
 378 is presented in Figure 3 for the 26 sites at latitudes  $\lambda = 60^\circ–70^\circ\text{N}$ . This figure shows that in the pre-midnight hours  
 379 the frequency of occurrence is greatest near the equinoxes, when the geomagnetic field is more favourably oriented  
 380 for reconnection with the IMF (Russell & McPherron, 1973; Zhao & Zong, 2012). However, for RMS fluctuations  
 381 (Figure 3e–h), as  $\tau$  increases from 1 min to 60 min, the greatest frequency of occurrence occurs on the dawn side  
 382 (03–09 MLT). We also note, for both  $R_1$  and  $S_1$  distributions, a change in the locus of peak occurrence from 04–  
 383 05 MLT near the summer solstice to 07–08 MLT near the winter solstice, which may be associated with changes  
 384 in the position of the dawn terminator at these latitudes and the seasonal changes in the geometry of the  
 385 geomagnetic field relative to the IMF. For  $\tau \geq 10$  min, however, the frequency of occurrence in the winter months  
 386 (December and January) is reduced relative to that for  $\tau = 1$  min, in both  $R_n$  and  $S_n$ , and this also limits the time  
 387 zones of occurrence in the late morning.



388 Figure 3.  $\text{Pr}(|dB_h/dt| > P_{99.97})$  vs (MLT, month) for (a)  $R_1$ , (b)  $R_{10}$ , (c)  $R_{30}$ , (d)  $R_{60}$ , (e)  $S_1 (= R_1)$ , (f)  $S_{10}$ , (g)  
 389  $S_{30}$ , (h)  $S_{60}$  for stations between 60 – 70°N CG latitude.

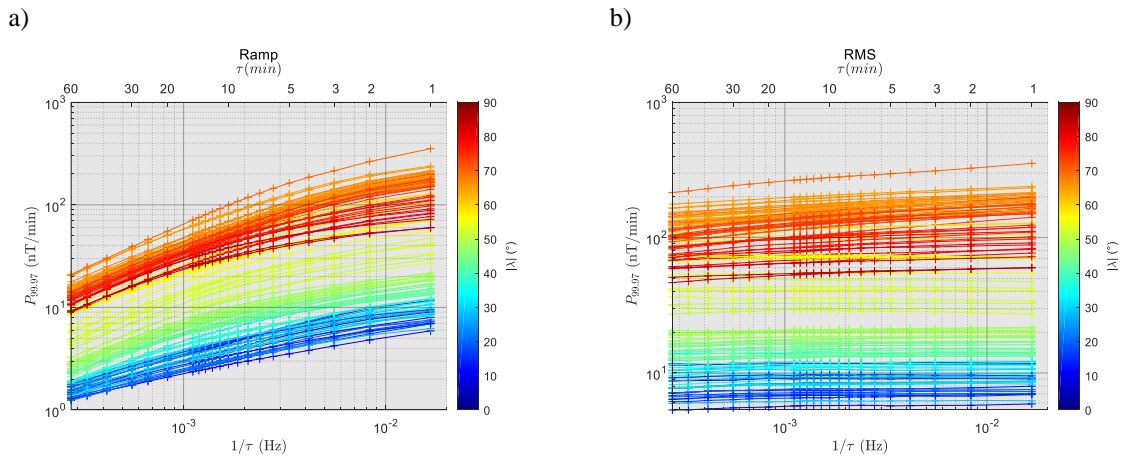
## 390 4 The frequency and latitude dependence of $R_n$ and $S_n$

### 391 4.1 Modelling the 99.97<sup>th</sup> percentile

392 We now develop a model for the geomagnetic fluctuation amplitude as a function of sampling frequency and  
 393 geomagnetic latitude, first for the 99.97<sup>th</sup> percentile of  $|dB_h/dt|$  and in Section 4.2 for predicted 100-year return  
 394 level estimates. Figure 4 presents  $P_{99.97}$  as a function of sampling frequency,  $f_s = 1/\tau$  for a)  $R_n$ , and b)  $S_n$  at each  
 395 of 125 magnetometer sites. The colour of each line indicates the absolute CG latitude of the site,  $|\lambda|$ , and the upper  
 396 horizontal scale indicates the sampling period,  $\tau$ . Since the axes are logarithmic in both  $P_{99.97}$  and  $f_s$ , a straight  
 397 line with gradient  $p$  would indicate the power-law relation,  $P_{99.97}(f_s) \propto f_s^p$ , but it is clear from the curvature of  
 398 the lines, at least for ramp changes, that this is not an appropriate model and it is observed that the gradients,  
 399 curvature and offset vary with latitude. This was modelled by fitting a quadratic function,

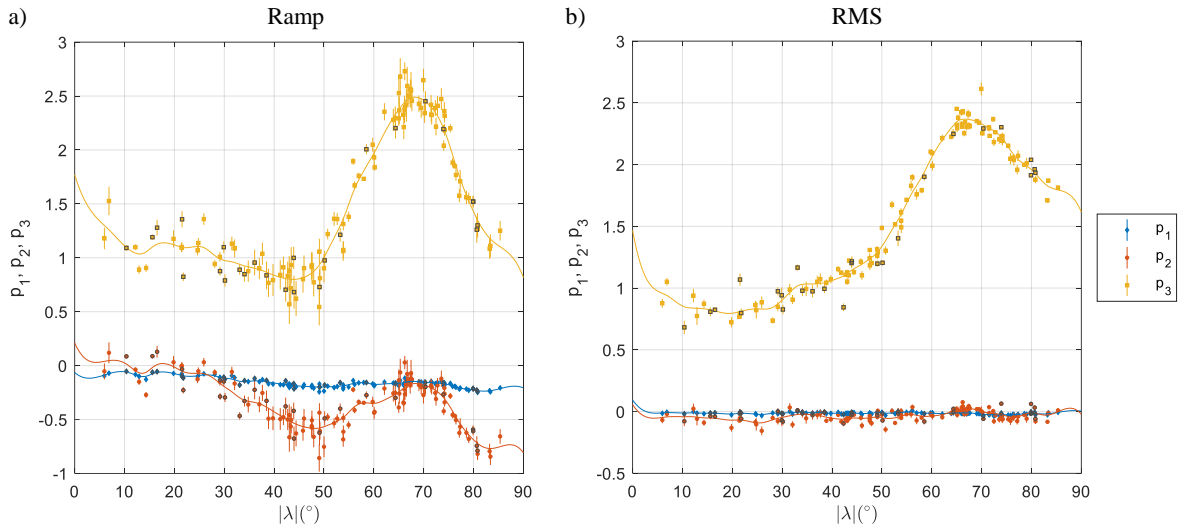
$$\mathbf{y} = p_1 \mathbf{x}^2 + p_2 \mathbf{x} + p_3 \quad (6)$$

400 where  $\mathbf{y} = \log(P_{99.97}(f_s))$  and  $\mathbf{x} = \log(f_s)$ .

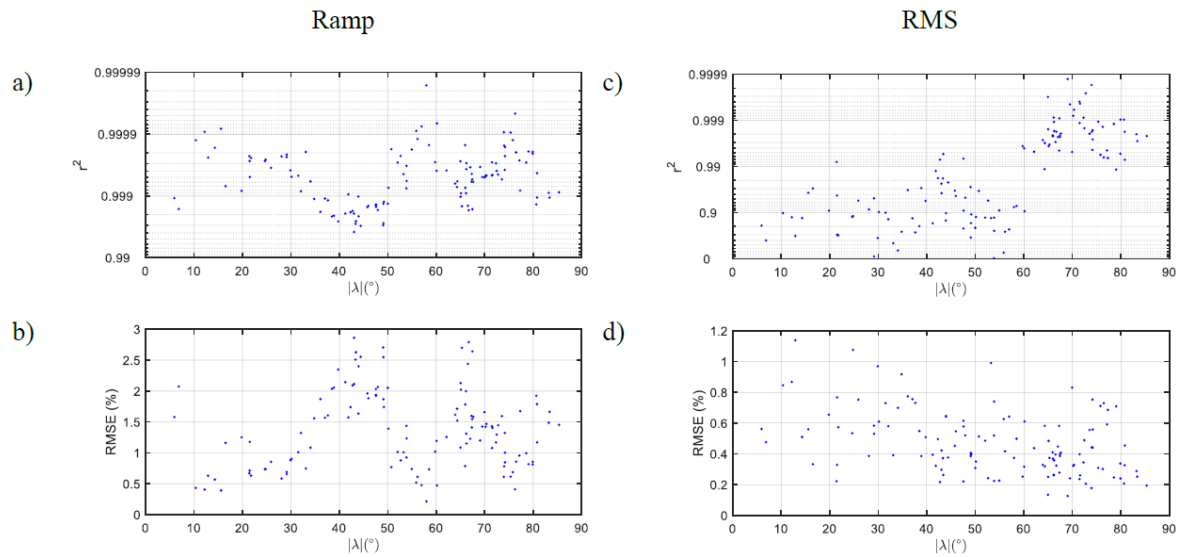


401 Figure 4. 99.97<sup>th</sup> percentiles of  $|dB_h/dt|$  for a) Ramp changes ( $R_n$ ) and b) RMS variation ( $S_n$ ) for 125 magnetometers, as  
 402 a function of sampling frequency,  $f_s = 1/\tau$ , and coloured according to absolute CG latitude,  $|\lambda|$ .

403 The best-fit quadratic coefficient,  $p_1$  linear coefficient,  $p_2$ , and constant term,  $p_3$ , are presented in Figure 5 as a  
 404 function of  $|\lambda|$ . Here the error bars are 95% confidence intervals (CI). The distributions are approximately  
 405 symmetric about the geomagnetic equator ( $\lambda = 0$ ). We have fitted smoothing splines (solid curves) using the  
 406 absolute CG latitude as the dependent variable (i.e. fitting to  $p_k(|\lambda|)$ , for  $k = 1,2,3$ ) and weighting each point by  
 407 the inverse of the 95% CI. The constant terms ( $p_3$ ) have broad maxima in the auroral zones, as expected from  
 408 Figure 1. However, for ramp changes (Figure 5a), the linear and quadratic coefficients ( $p_2$  and  $p_1$ ) also show a  
 409 strong dependence on  $|\lambda|$ . For RMS fluctuations (Figure 5b), the changes in  $p_2$  and  $p_1$  are much less significant.  
 410 The smoothing spline fits to the coefficients thus provide a global model for the 99.97<sup>th</sup> percentiles of  $R_n$ , and  $S_n$ .



411 Figure 5. Coefficients of the polynomial (6) fitted to  $\log P_{99.97}(\log f_s)$  at 125 magnetometers, for a)  $R_n$ , and b)  $S_n$  as a  
 412 function of absolute CG latitude. Markers for Southern Hemisphere sites have a grey outline. Error bars indicate 95% CIs.  
 413 Solid lines indicate smoothed spline fits to  $p_k(|\lambda|)$ , for  $k=1,2,3$  with points weighted by  $1/\text{CI}$ . Units of  $p_k$  are  $(10 \text{ dB nT min}^{-1} \text{ deg.}^{-k-3})$ .  
 414



415  
 416 Figure 6. Goodness-of-fit metrics for the polynomial fit to  $\log P_{99.97}(\log f_s)$  for (a, b) Ramp changes, and (c,d) RMS  
 417 variations. Top panels (a,c) are coefficients of determination,  $r^2$ . Bottom panels (b,d) are the RMS of residuals.

418 The goodness of the quadratic fits at each magnetometer site are presented in Figure 6 for 99.97<sup>th</sup> percentiles of  
 419  $R_n$  (left panels, a and b) and  $S_n$  (right panels, c and d). Panels (a) and (c) present the coefficients of determination,  
 420  $r^2$ . To better illustrate values of  $r^2$  close to 1, the vertical axis scaling in panels a and c is “inverse logarithmic”  
 421 such that a set of values,  $r^2 = 1 - 10^{-m}$  would be uniformly spaced for uniformly spaced  $m$ . Panels (b) and (d)  
 422 present the RMS percentage error (i.e. the RMS value of  $100\% \times (\hat{P}_{99.97} - P_{99.97})/P_{99.97}$ , where  $\hat{P}_{99.97}$  are the  
 423 model estimates). The quadratic models for  $R_n$  fit well, with  $r^2 > 0.99$  for all sites (see panel a), and RMS residuals  
 424 less than 3%. The quadratic model for  $S_n$  fits well at high latitudes ( $|\lambda| > 60^\circ$ ), with  $r^2 > 0.99$  (panel c), and for  
 425 all sites the RMS of residuals is very low ( $< 1.2\%$ ).

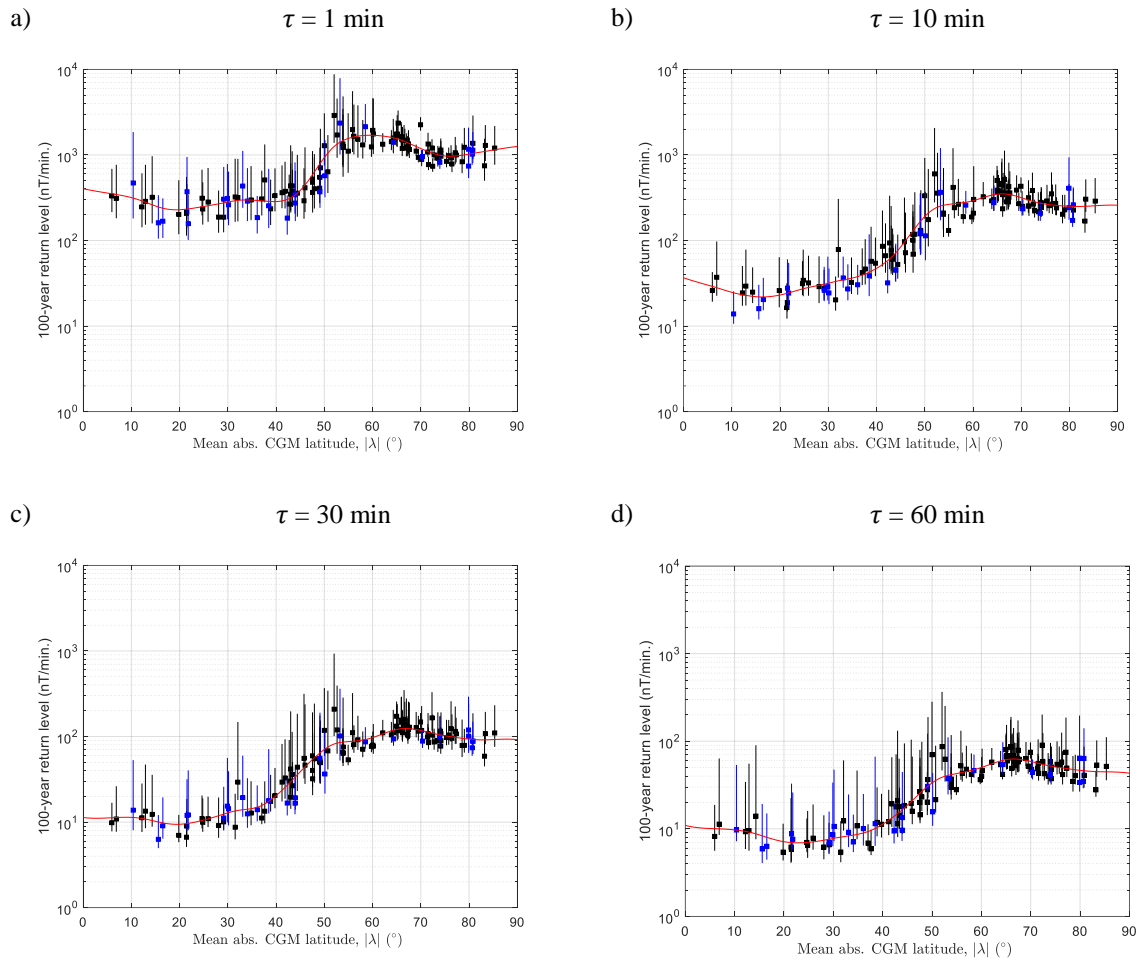
## 426 4.2 Modelling return levels

427 Generalised Pareto (GP) distribution functions were fitted to exceedances of  $R_n$  above a  $P_{99.97}$  threshold (after  
 428 12-h run-length declustering above the same threshold) independently for each magnetometer site. 100-year return  
 429 levels of  $R_n$  were then determined from the GP distribution at a probability level equivalent to a 1-in-100 years  
 430 of observations. A numerical method was used to determine a maximum likelihood estimate (MLE) for the return  
 431 level with 95% confidence intervals determined from the (asymmetric) log-likelihood profile, as described in  
 432 (Gilleland & Katz, 2016). This procedure was repeated for all 125 magnetometer sites and the results are plotted  
 433 against  $|\lambda|$  in Figure 7. Panels a, b, c and d, present 100-year return levels of  $R_n$  for  $n = 1, 10, 30,$  and 60 (minutes),  
 434 respectively; points represent MLEs (coloured blue for southern hemisphere sites, black for northern hemisphere)  
 435 with error bars indicating the 95% CI. The red curve in each panel is a smoothing-spline interpolation to the MLE  
 436 values. In Figure 8 the interpolating spline curves are presented for return periods from 5 to 500 years.

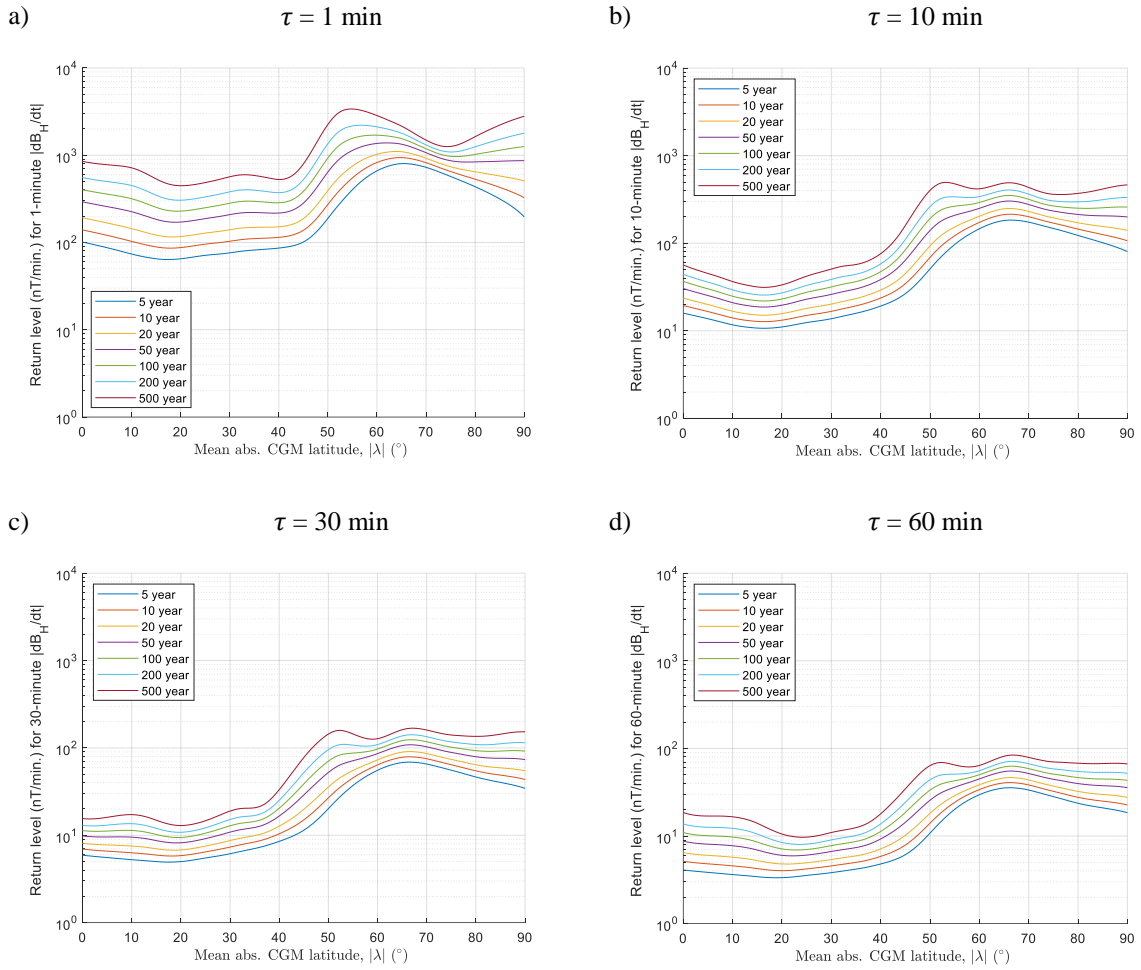
437 The 100-year return levels for  $R_1$  (Figure 7a) (1-minute ramp changes) are distinctly elevated for sites around  
 438  $|\lambda| \cong 52\text{--}54^\circ$  and reference to Figure 8 indicates that the latitude of this maximum decreases with increasing  
 439 return period. This indicates that the extreme  $R_1$  events (declustered threshold exceedances) that occur less  
 440 frequently (i.e. with longer return periods) have greater amplitude and occur at lower absolute latitudes. This  
 441 pattern of behaviour could indicate that largest and rarest auroral current fluctuations occur during substorm  
 442 expansions associated with brightening auroral arcs at the equatorward edge of a greatly expanded auroral oval  
 443 (i.e. following a large substorm growth phase). Over 10–60 minute timescales (Figure 7b to d) the peak near  $53^\circ$   
 444 is still present but less pronounced, and Figure 8b–d shows that it has similar or lower magnitude than the broad  
 445 peak around  $|\lambda| \cong 67^\circ$  that was observed in the  $P_{99.97}$  profiles (Figure 1a).

446 The same procedure of fitting GP distribution functions was used to determine extreme values for the RMS  
 447 variation over  $n$ -minute periods,  $S_n$ . Figure 9 presents the 100-year return levels and Figure 10 presents the  
 448 smoothed-spline fits for 5–500 year return periods for the  $S_n$ , again for periods of  $\tau = 1, 10, 30,$  and 60 minutes,  
 449 The shape of these distributions are very similar to those of the  $R_n$  fluctuations although the reduction in level  
 450 with increasing  $\tau$  is much less pronounced.

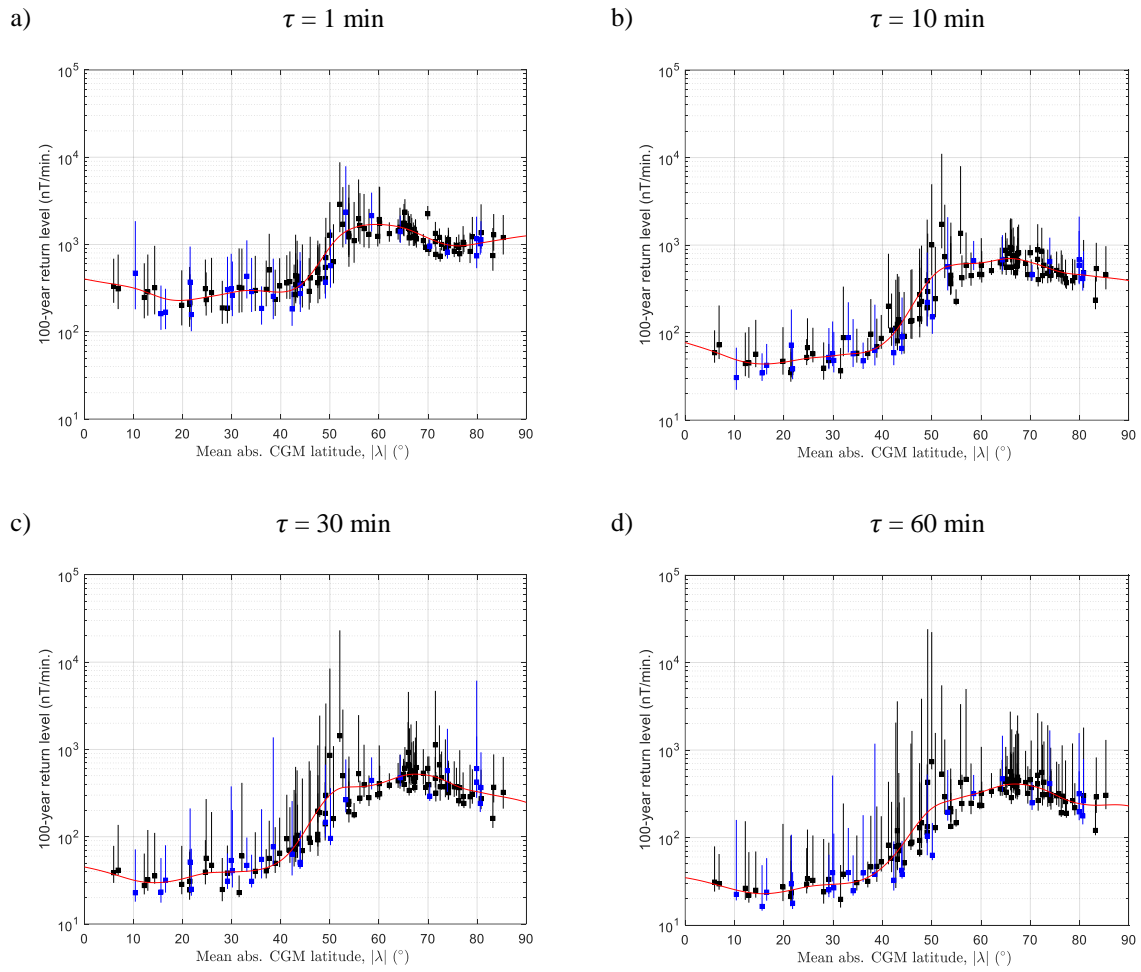
451 For both  $R_n$  and  $S_n$  metrics (Figure 8 and Figure 10, respectively) there is an increase in RLs towards the equator,  
 452 potentially associated with activity in the equatorial electrojet current systems, and for return periods greater than  
 453 100 years there is a predicted increase in RL as latitude  $|\lambda|$  increases above  $74^\circ$ , for  $\tau = 1$  and 10 min.



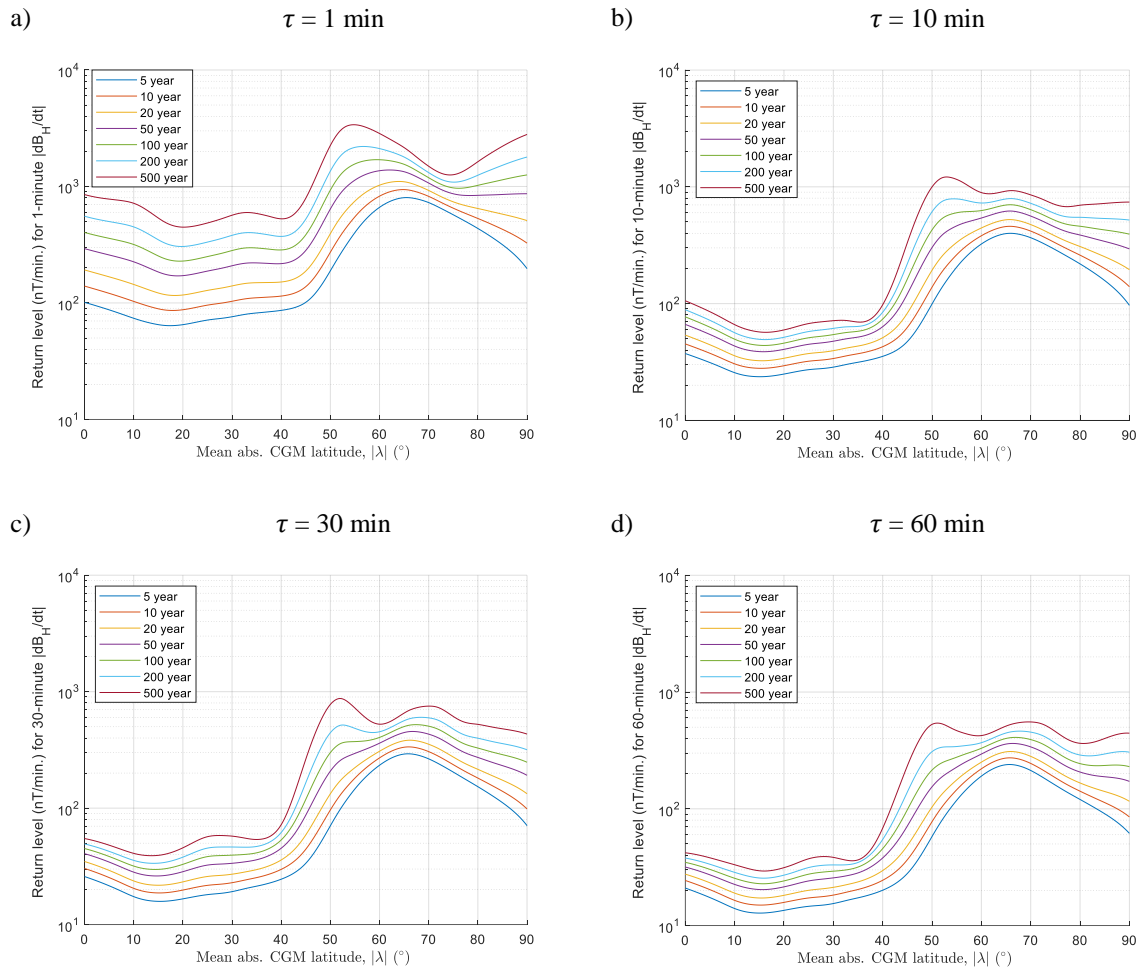
454 Figure 7. 100-year return levels (Max. likelihood estimates with 95% CI shown as error bars) for ramp changes ( $R_n$ )  
 455 estimated from GP distributions fitted above  $P_{99.97}$ . Black indicates NH sites, blue indicates SH. a)  $\tau = 1$  min, b)  $\tau = 10$  min,  
 456 c)  $\tau = 30$  min, and d)  $\tau = 60$  min. The red curves are smoothed spline fits to MLEs.



457 Figure 8. Smoothed spline fits to return levels of Ramp changes ( $R_n$ ), as shown by the red curve in Figure 7 (100-year  
 458 Return Period), but repeated for a range of return periods. a)  $\tau = 1$  min, b)  $\tau = 10$  min, c)  $\tau = 30$  min, and d)  $\tau = 60$  min.



459 Figure 9. 100-year return levels (Max. likelihood estimates with 95% CI shown as error bars) for RMS variations ( $\mathcal{S}_n$ ). Black  
 460 indicates NH sites, blue indicates SH. a)  $\tau = 1$  min, b)  $\tau = 10$  min, c)  $\tau = 30$  min, and d)  $\tau = 60$  min. The red curves are  
 461 smoothed spline fits to MLEs.

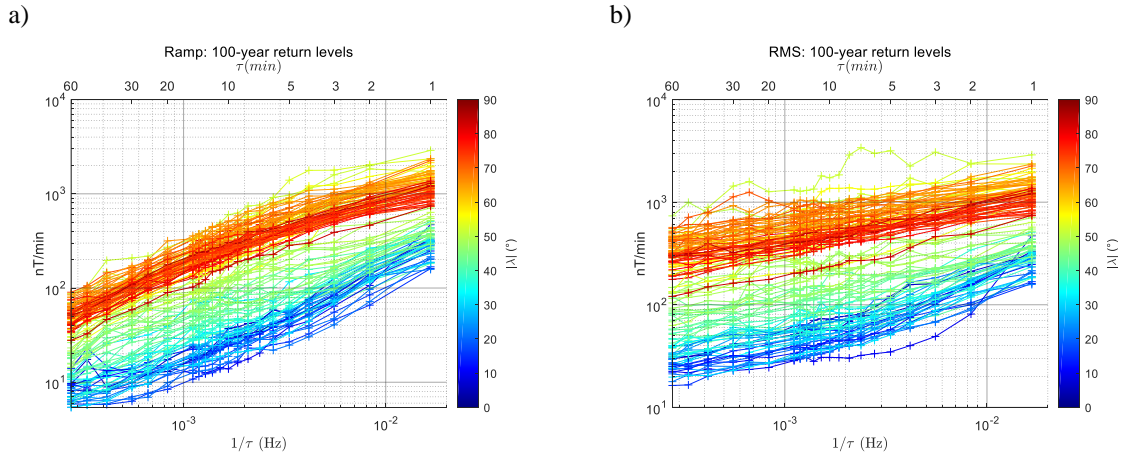


462 Figure 10. Smoothed spline fits to return levels of RMS variation ( $S_n$ ), as shown by the red curve in Figure 9 (100-year  
 463 Return Period), but repeated for a range of return periods. a)  $\tau = 1$  min, b)  $\tau = 10$  min, c)  $\tau = 30$  min, and d)  $\tau = 60$  min.

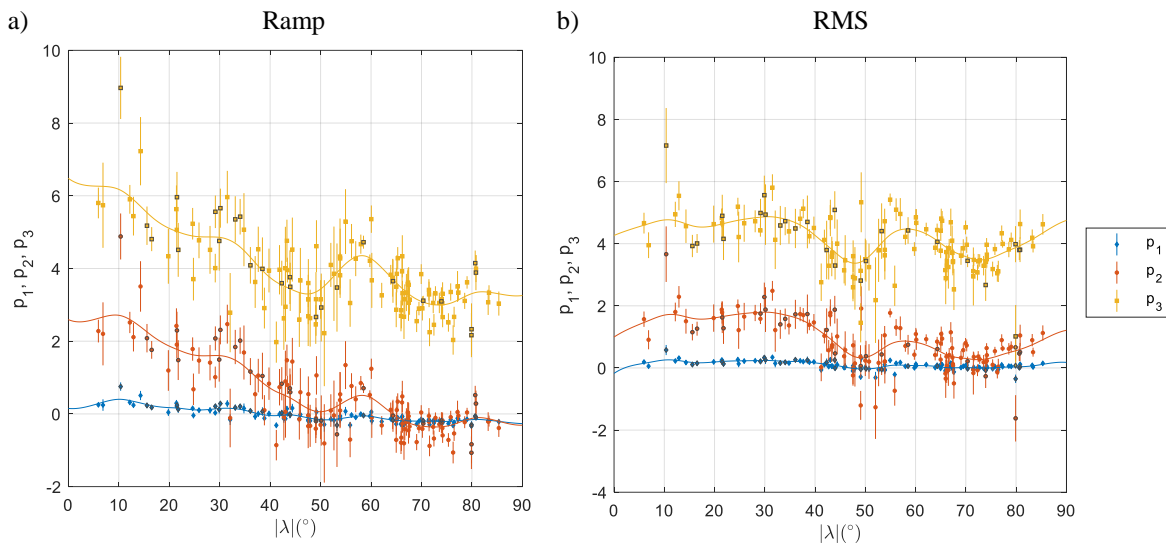
464 The return level predictions presented above should be interpreted with caution for return periods of 100 years or  
 465 more (i.e. well in excess of the duration of measurements). Our analysis is based purely on the statistical temporal  
 466 properties of measurements at individual magnetometer sites and we have not attempted to model the spatial  
 467 variation in the probability distributions. Magneto-hydrodynamic modelling (e.g. Ngwira et al., 2014) has  
 468 indicated that the intense auroral electrojet currents that drive extreme values of  $R_n$  and  $S_n$  may, under extreme  
 469 solar conditions, extend much further equatorward than suggested by our results, and historical records suggest  
 470 that auroras during the September 1859 ‘Carrington’ storm would have been observed at the zenith at  $31^\circ\text{N}$   
 471 geomagnetic (Cliver & Dietrich, 2013). The measurements at low-latitude sites contain no observations of such  
 472 extreme conditions and therefore may indicate misleadingly low return levels. Similar situations (in which more  
 473 severe events tend to be spatially more localised) are frequently encountered in environmental and geospatial data  
 474 sets and advanced methods for analysing such ‘spatial extremes’ are reviewed by Hüser & Wadsworth (2020).

475 We now present models of the MLEs of 100-year return levels of  $R_n$  and  $S_n$  as functions of sampling frequency,  
 476  $f_s$ , and absolute CG latitude,  $|\lambda|$ , following the same procedure as for the  $P_{99.97}$  levels developed in Section 4.1.  
 477 Figure 11 presents 100-year RLs for a)  $R_n$  and b)  $S_n$ , in the same format as Figure 4. The coefficients of the  
 478 polynomials (6) fitted to the return levels are presented in Figure 12. The 95% CI of the fitted coefficients (error  
 479 bars in Figure 12) are larger than for the  $P_{99.97}$  model, but the profiles remain approximately symmetric about  $\lambda =$

480  $0^\circ$ . It is interesting to note for the ramp changes,  $R_n$ , there is a pronounced change from positive to negative  
 481 curvature as  $|\lambda|$  increases, which can be seen in the profiles of Figure 11 and the change in quadratic coefficient,  
 482  $p_1$ , in Figure 12. For both  $R_n$  and  $S_n$ , the gradients (or the linear coefficients,  $p_2$ ) are significantly higher at lower  
 483 latitude  $|\lambda|$ .

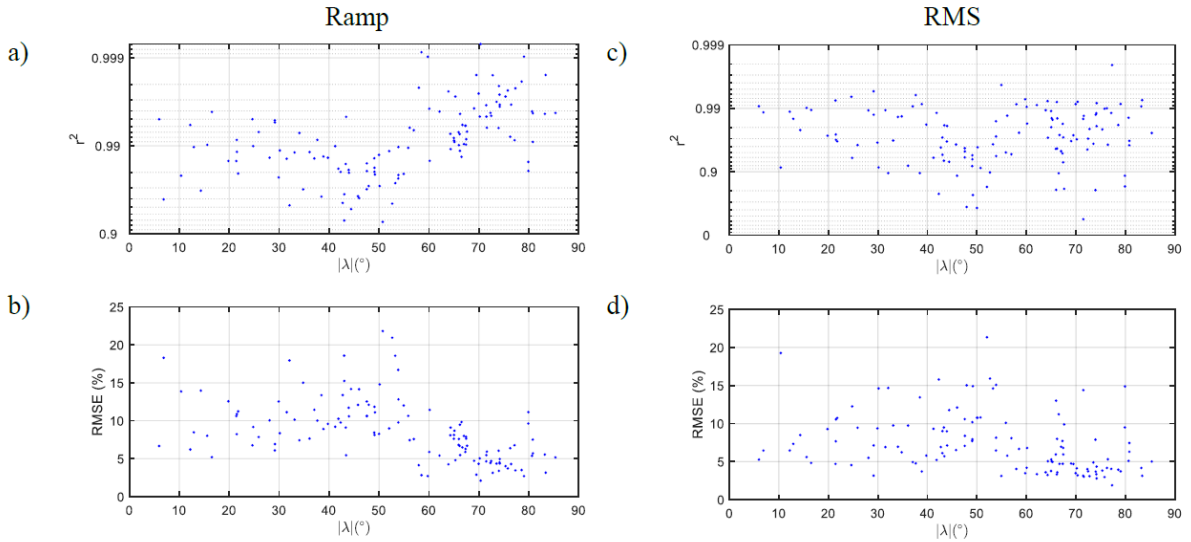


484 Figure 11. 100-year return levels for a)  $R_n$ , and b)  $S_n$ , for  $n = 1-60$  min (top axis), plotted against the sampling frequency  
 485 (bottom axis). MLE values are shown for all 125 magnetometer sites, coloured according to absolute geomagnetic latitude,  
 486  $|\lambda|$ .



487 Figure 12. Coefficients of the polynomial (6) best fitted to 100-year return levels of  $|dB_n/dt|$ , presented in the same format  
 488 as Figure 5. a)  $R_n$ , and b)  $S_n$ . Markers for Southern Hemisphere sites have a grey outline.

489 Figure 13 provides goodness-of-fit metrics for the polynomials (6) fitted to MLE of  $RL_{100}$ , presented in the same  
 490 format as Figure 6. Not unexpectedly,  $RL_{100}$  shows greater variation from the polynomial model than  $P_{99.97}$  (cf.  
 491 Figure 6) but in the vast majority of cases the RMS errors are still less than 15% and have a coefficient of  
 492 determination greater than 0.9.



493

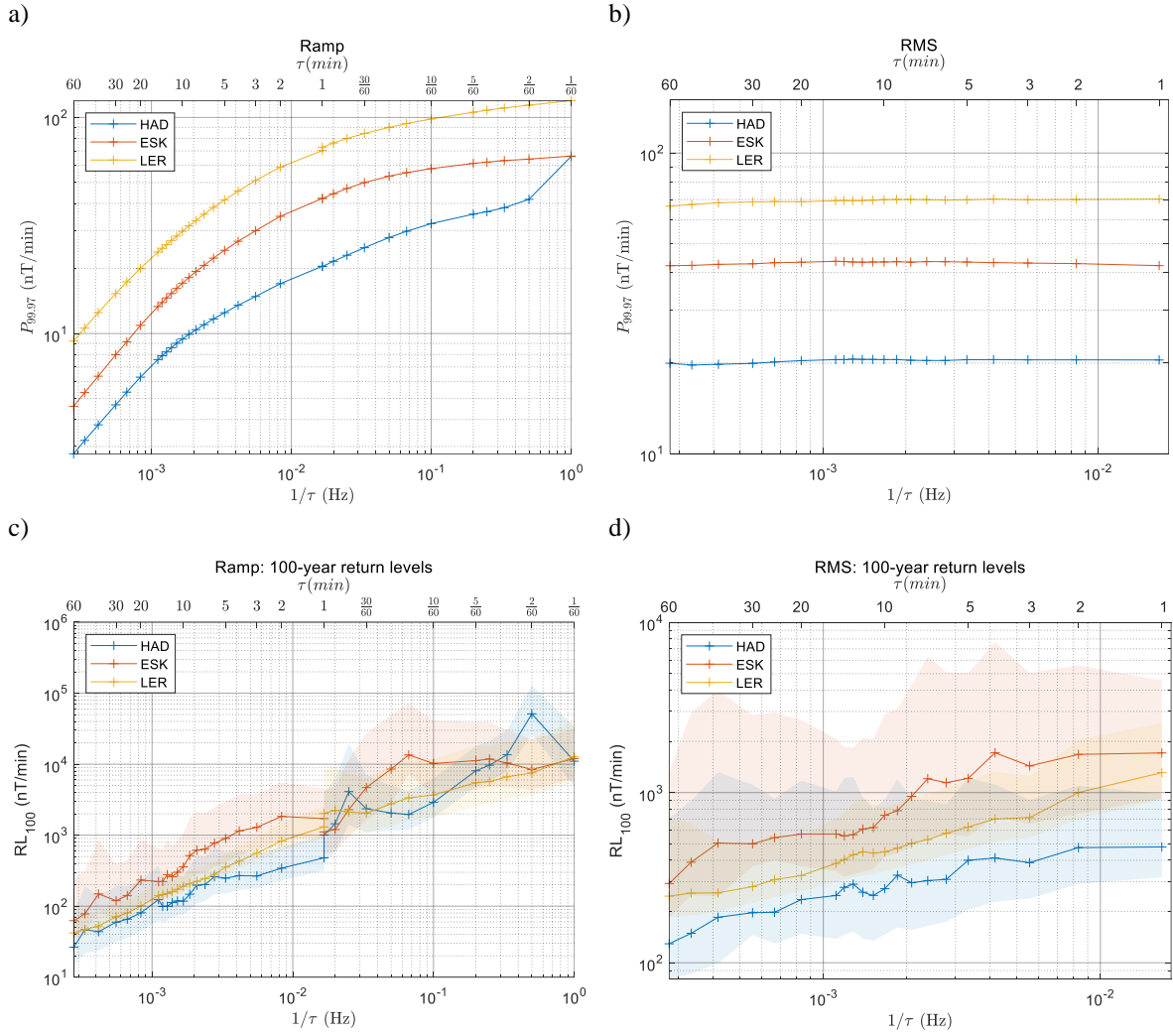
494 Figure 13. Goodness-of-fit metrics for the polynomial (6) fit to  $\log RL_{100}(\log f_s)$  for (a,b) Ramp, and (c,d) RMS

495 fluctuations. Top panels (a,c) are coefficients of determination,  $r^2$ . Bottom panels (b, d) are the RMS of residuals.

496

### 497 4.3 Predictions of extreme geoelectric fields in the UK

498 We shall now focus on the statistics for three UK magnetometer sites, HAD, ESK and LER. Figure 14 presents,  
 499 for each site, the 99.97<sup>th</sup> percentiles of a)  $R_n$ , and b)  $S_n$ , and 100-year return levels for c)  $R_n$ , and d)  $S_n$ . For the  
 500 ramp changes,  $R_n$  (Figure 14a and c) the frequency scale is extended up to 1 Hz using the 1-s cadence dataset.  
 501 Whilst the length of the datasets differ for 1-s and 1-min data, the discontinuities in the  $P_{99.97}$  curves (Figure 14a)  
 502 at  $\tau = 1$  min are negligible, although a larger discontinuity arises from the RL estimates (Figure 14c). Statistics  
 503 for  $S_n$  (Figure 14b and d) could not be extended to 1 Hz since they are defined from 1-min cadence measurements  
 504 (Equation (4)), but they are presented here for  $\tau = 1$ -60 min to illustrate that whilst the 99.97<sup>th</sup> percentile varies  
 505 little with sample frequency (panel b), their 100-year RLs (panel d) have a much more significant frequency  
 506 dependence, albeit with large 95% confidence intervals (illustrated by the shaded regions).



507 Figure 14. a)  $P_{99.97}$  of  $R_n$ , b)  $P_{99.97}$  of  $S_n$ , c) 100-year RLs of  $R_n$ , and d) 100-year RL of  $S_n$ , for three UK sites. RLs are  
 508 maximum likelihood estimates, whilst the shaded regions indicate 95% confidence intervals.

509 To derive estimates of the  $P_{99.97}$  and 100-year return levels of the geoelectric field from statistics of the  
 510 geomagnetic field, we make use of the MT transfer functions,  $\mathbf{Z}(f)/\mu$  measured at each UK site, as described in  
 511 Section 2. In Figure 15 (panels a, c, e) we present, for each site, the ‘apparent resistivity’ associated with each of  
 512 the four components of the observed  $\mathbf{Z}/\mu$ , defined as

$$\rho_{a(ij)} = \frac{\mu_0}{2\pi f} \left| \frac{Z_{ij}}{\mu} \right|^2 \quad (7)$$

513 where  $(Z_{ij} = Z_{xx}, Z_{xy}, Z_{yx}, Z_{yy})$  are the components of the impedance matrix,  $\mathbf{Z}$ . Figure 15 panels b, d and f show  
 514 the phases of  $Z_{ij}$ . Apparent resistivity is the resistivity of an electrically homogeneous and isotropic half-space  
 515 of permeability  $\mu = \mu_0$  (the permeability of free space) that would be consistent with the measured  $\mathbf{E}$  and  $\mathbf{B}$  fields.  
 516 Cagniard (1953) and Pirjola (1982) showed that, using a simple half-space model of the surface, an  
 517 electromagnetic wave polarised in the N-S plane, at the surface ( $z = 0$ ), the magnetic field

$$B_N = B_0 e^{i(2\pi f t - kz)} = B_0 e^{i2\pi f t} \quad (8)$$

518 would induce a geoelectric field,  $E$ , at the surface ( $z = 0$ ) of

$$E_E = - \sqrt{\frac{2\pi f}{\mu_0 \sigma}} B_N e^{i\pi/4} \quad (9)$$

519 in the east direction, where  $\sigma$  is the conductivity of the ground. Equation (9) is known as the “basic equation of  
 520 magnetotellurics” and is valid under the assumptions that the permittivity  $\epsilon \ll \sigma/2\pi f$  and the conductivity of the  
 521 air above the surface is negligible. As discussed by Wait (1962), the plane wave approximation (8) may be used  
 522 provided there is negligible change in the incident wave field amplitude over a lateral scale equal to the ‘skin  
 523 depth’ of the ground. Considering an additional orthogonal component of the magnetic field  $B_E$ , we may write (9)  
 524 more generally as

$$\begin{pmatrix} E_N \\ E_E \end{pmatrix} = \begin{pmatrix} 0 & Z \\ -Z & 0 \end{pmatrix} \begin{pmatrix} B_N \\ B_E \end{pmatrix} / \mu_0 \quad (10)$$

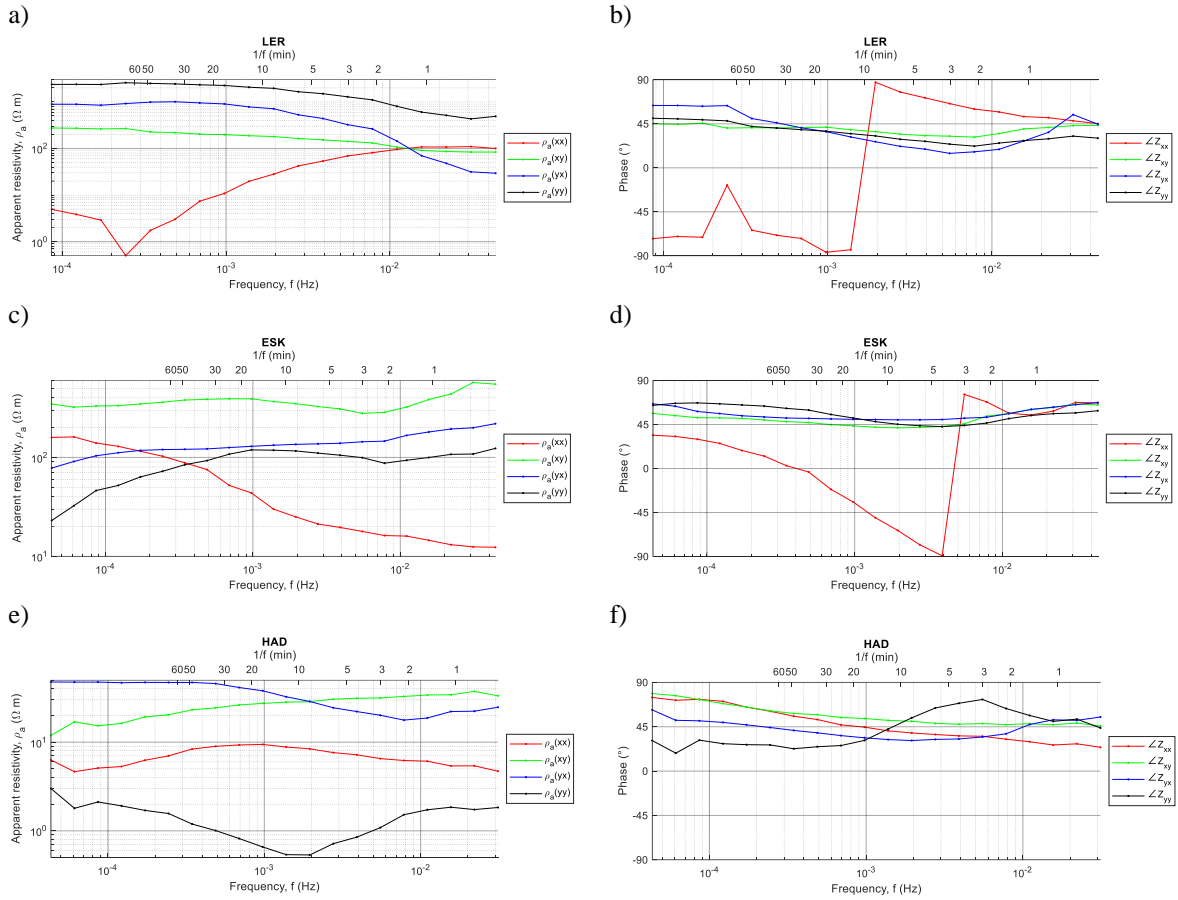
525 where

$$Z = \sqrt{\frac{2\pi f \mu_0}{\sigma}} e^{i\pi/4} \quad (11)$$

526 Thus, for a uniform half-space model earth,  $\rho_a$  would be invariant with frequency,  $f$ , and the components of  $Z$   
 527 would have a constant  $45^\circ$  phase for all  $f$ . The measurements in Figure 15 show that the apparent resistivity of  
 528 the ground differs greatly between sites as is expected from the very different geological settings that give rise to  
 529 the electrical response.

530

531



532 Figure 15. Apparent resistivity and phase of  $\mathbf{Z}$ , determined empirically for a-b) LER, c-d) ESK, and e-f) HAD magnetometers.  
 533 Panels (a, c, e) show the apparent resistivity, and panels (b, d, f) show the phase.

534 For each site, the off-diagonal components  $\rho_{a(xy)}$  and  $\rho_{a(yx)}$  are not of equal magnitude, which indicates that the  
 535 MT transfer function introduces ‘directional anisotropy’ (i.e. from Equation (10),  $|E_N| \neq |E_E|$  when  $|B_N| = |B_E|$ ).  
 536 The diagonal terms  $\rho_{a(xx)}$  and  $\rho_{a(yy)}$  are non-zero (notably for Lerwick), suggesting some deviation from the  
 537 simple half-space model (i.e. measurements imply a fully three-dimensional distribution of electrical resistivity).

538 Noting from (8) that

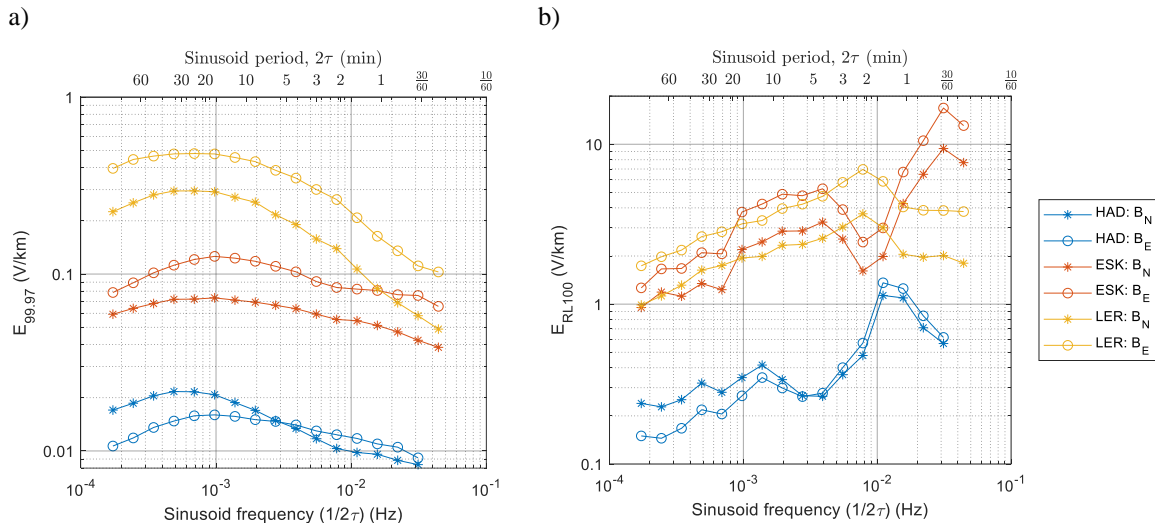
$$\frac{dB_N}{dt} = i2\pi f B_N \quad (12)$$

539 and similarly for  $B_E$ , we may estimate the geoelectric field from the rate-of-change of the magnetic field:

$$\mathbf{E}(f) = \frac{1}{i2\pi f} \mathbf{Z}(f) \begin{pmatrix} \frac{dB_N}{dt}(f) \\ \frac{dB_E}{dt}(f) \end{pmatrix} \quad (13)$$

540 where  $\mathbf{Z}$  is determined from the empirical MT transfer function ( $\mathbf{Z}/\mu$ ) using the approximation  $\mu \cong \mu_0$ . In the  
 541 ideal case of homogenous ground conductivity, equations (13) and (11) indicate that the spectrum of  $|E|$  is  
 542 proportional to  $f^{-0.5}$  times the spectrum of  $|dB/dt|$  (i.e. it is low-pass filtered).

543 To estimate the amplitude of the geoelectric field expected to result from the 99.97<sup>th</sup> percentile of  $R_n$  for a range  
 544 of frequencies, we modelled the waveform as a vertically propagated sinusoid  $B_0 \sin(2\pi f)$  with amplitude  $B_0 =$   
 545  $\tau P_{99.97}/2$  and frequency  $f = 1/(2\tau)$ . This required a linear interpolation of the  $P_{99.97}$  (Figure 14a) to frequencies  
 546 recorded in the MT transfer function at each site (Figure 15). The resulting estimates of the magnitude  $|E| =$   
 547  $\sqrt{E_N^2 + E_E^2}$  from Equation (13) are presented in Figure 16a where circles represent  $B$ -field fluctuations confined  
 548 to the N-S plane ( $|B_N| = B_0$ ;  $B_E = 0$ ) and asterisks represent  $B$ -field fluctuations in the E-W plane ( $B_N = 0$ ;  
 549  $|B_E| = B_0$ ). The two polarisations yield  $E$ -fields that differ in magnitude by a factor of up to 2 because the MT  
 550 transfer function is not directionally isotropic and the ground impedance depends on all three coordinates ( $x, y,$   
 551  $z$ ). At each UK site, exceedances of  $P_{99.97}$ , after declustering, occurred on average every 0.1 to 0.35 years over  
 552 the range  $\tau = 1$  to 60 min, and so should be considered as large, but not extreme values. Figure 16b presents the  
 553  $E$ -field magnitude for sinusoids with peak-to-peak amplitude ( $2B_0$ ) equal to the 100-year return levels,  $R_n$  (from  
 554 Figure 14c).



555 Figure 16. a) 99.97<sup>th</sup> percentile and b) 100-year RL of  $|E|$  at three UK sites. Circles indicate fields modelled with sinusoidal  
 556  $B$ -field in the N-S plane, asterisks are for  $B$  in the E-W plane.

557 To put these values in context, an  $E$  field of 1–2 V/km over large distances can, depending on the grid topology,  
 558 produce GIC that saturates the steel core of a high-voltage transformer, which may lead to heating and potential  
 559 failure of core components and the introduction of harmonics in the power system (Barnes et al., 1991). Winter et  
 560 al. (2017) estimated the  $E$  field at UK latitudes associated with the 1859 storm – the largest geomagnetic storm  
 561 on record (Carrington, 1859; Cliver & Dietrich, 2013) – to be approximately 9 V/km, and it is estimated that the  
 562 nine-hour Hydro-Québec electricity blackout of March 1989 resulted from  $E$  fields of about 10 V/km (Barnes et  
 563 al., 1991).

564 The predicted frequency dependences for the 99.97<sup>th</sup> percentile of  $|E|$  (denoted  $E_{99.97}$ ) take a very different form  
 565 to those for the 100-year return levels (denoted  $E_{RL100}$ ):  $E$ -field amplitudes at the 99.97<sup>th</sup> percentile (occurring  
 566 several times a year) are greatest for sinusoid periods of approximately 20 min, whilst 1/100 year events have  
 567 greatest amplitude for periods between 30 s and 2 min. The observation that 100-year RL predictions vary greatly  
 568 with sinusoid frequency has important implications when comparing and contrasting statistical studies evaluating  
 569 extremes of  $|E|$  which may have been based on different sinusoid frequencies.

570 Model estimates of the  $E$  field based on single-frequency components of the geomagnetic fluctuation have been  
571 reported by several authors (Beggan et al., 2013; Beggan, 2015; Bedrosian and Love, 2015; Love et al., 2016b).  
572 Love et al. (2016b) examined the amplitude of 4-min period sinusoids fitted to geomagnetic measurements (over  
573 sliding 10-min windows) and estimated extreme  $E$ -field amplitudes using empirical MT transfer functions at sites  
574 in the contiguous USA ( $\lambda \cong 40\text{--}60^\circ\text{N}$ ). Only at the northern limit, in the northern mid-west states, did they find  
575  $E_{RL100}$  exceeding 3 V/km, which is similar to the 3-5 V/km predicted in Figure 16 for LER ( $\lambda = 58^\circ\text{N}$ ) for a 4-  
576 min sinusoid period. However, direct comparisons between sites cannot be made without considering differences  
577 in the surface impedance and its gradients. Bedrosian and Love (2015) illustrated this point by simulating the  $E$   
578 fields generated by sinusoids with 10-, 100-, and 1000-s periods using MT transfer functions from the EarthScope  
579 MT array in the Midwest USA and showed that a constant-amplitude  $B_0 = 500$  nT, 100-s period  $B$  field would  
580 induce  $|E|$  of 2.7 V/km, averaged across all sites, but with values ranging from 0.15 to 16.8 V/km depending on  
581 site. Similarly, Pulkkinen et al. (2012), by extrapolating a log-normal distribution of 10-s field data from 23  
582 European sites ( $55^\circ\text{--}75^\circ\text{N}$  geomagnetic), predicted  $E_{RL100}$  ranging from 5V/km with a high-conductivity ground  
583 model, to 20 V/km for poor-conductivity ground. Beggan et al. (2013) and Beggan (2015) also modelled the  
584 extreme  $E$ -field in the UK based on a conductivity model and  $B$ -fields modelled as sinusoids with periods,  $T$ , of  
585 2, 10 and 30 minutes and amplitudes based on the 30-, 100-, and 200-year return levels of 1-min  $dB_h/dt$  predicted  
586 by Thomson et al. (2011). The 2-min  $E_{RL100}$  prediction of Beggan et al. (2013) shown in their Fig. 6 (middle  
587 column) shows not only the high level of localisation of the  $E$  field intensity, ranging from around 2 to 7 V/km,  
588 but also the importance of the direction of the inducing  $B$ -field (whether N-S or E-W aligned) for some locations.  
589 We intend to report further on the importance of directionality in extreme  $dB_h/dt$  statistics in a forthcoming  
590 publication.

591 There are, of course, limitations to ‘narrowband’ models of geomagnetic events since, in practice, fluctuations  
592 will be broadband in nature and the frequency spectrum of any individual geomagnetic event will be unique. We  
593 have noted that many of the extreme events (exceeding  $P_{99,97}$ ) identified in our dataset occur simultaneously  
594 (within hours of each other) over a wide range of timescales (or frequencies), but our results should not be used  
595 to infer a frequency spectrum of  $B$  or  $E$  fields for any given extreme geomagnetic event. For this information the  
596 reader may refer to several studies of extreme values that have taken the approach of analysing the  $E$  field  
597 produced during rare and intense geomagnetic storm periods and in some cases scaling up their effect to simulate  
598 100-year return levels (e.g. Ngwira et al., 2013; Pulkkinen et al. 2012; Lotz & Danskin, 2017).

## 599 5 Conclusion

600 The importance of ULF waves in driving extreme geoelectric fields and GICs has received a great deal of interest  
601 in recent years (Hartinger et al., 2020; Belakhovsky et al. 2019; Heynes et al. 2020; Pulkkinen & Kataoka, 2006)  
602 and there is a need for better understanding of the frequency dependence of the  $B$  and  $E$  field fluctuations driving  
603 GICs (e.g. Pulkkinen et al., 2017). Most previous statistical climatological studies of extreme values for  $E$  and  
604  $dB_h/dt$  have been based on sampling at just one or two frequencies. In this paper, however, we have presented  
605 statistics of large ( $P_{99,97}$ ) and extreme (e.g. 1/100-year) values for  $|dB_h/dt|$  on a wide range of timescales,  $\tau$ ,  
606 from 1 to 60 min. At latitudes above the dayside cusp ( $\lambda > 80^\circ$ ), for example, we find that occurrences of  $|dB_h/dt|$   
607 ramp changes above  $P_{99,97}$  become tightly clustered in the few hours about local noon, and the effect is greatest

608 for longer timescales ( $\tau \geq 30$  min). We have contrasted the statistics of ramp changes with those of the RMS of  
 609 1-min fluctuations over the same range of timescales and find, in particular, that in the auroral zone, for  $\tau > 10$   
 610 min the MLT of greatest occurrence of large RMS variation is from dawn to noon, indicative of strong ULF wave  
 611 activity in this local time sector. The frequency ( $1/\tau$ ) dependences (for both ramp changes and RMS variations)  
 612 are found to be not a simple power law, but are well modelled by quadratic functions whose three coefficients  
 613 vary predictably with geomagnetic latitude.

614 For three UK locations we extended the data set to 1 Hz sampling frequency and, using a plane wave  
 615 approximation and measured MT transfer functions, we derived the frequency dependence of the 99.97<sup>th</sup> percentile  
 616 and 100-year return levels of the geoelectric field,  $E$  at those sites. For events occurring several times a year (at  
 617 the 99.97<sup>th</sup> percentile) the induced  $E$  fields were greatest for fluctuations of 20-min period, whilst the 1-in-100-  
 618 year return levels were greatest for 0.5–2 min period fluctuations.

619 These statistics may be useful when inferring the likely extremes of  $|dB_h/dt|$  or  $E$  over a wide frequency range  
 620 based on studies that used a single sampling cadence. The distributions of extreme occurrence rates with latitude,  
 621 local time and season may also improve our understanding of the main ionospheric and magnetospheric drivers  
 622 of GICs.

## 623 **Annex A**

624 It is here demonstrated that the horizontal geoelectric field magnitude  $|E|$  is proportional to  $R_n$  as defined in  
 625 Equation (2) when using a half-space model for the impedance matrix. From Equation (10), the idealised half-  
 626 space impedance is given by

$$627 \quad \mathbf{Z} = \sqrt{\frac{2\pi f \mu_0}{\sigma}} e^{i\pi/4} \begin{pmatrix} 0 & 1 \\ -1 & 0 \end{pmatrix} \quad (A.1)$$

628 and for a sinusoidal horizontal magnetic field,  $\mathbf{B} \equiv \begin{pmatrix} B_N \\ B_E \end{pmatrix}$ , with frequency  $f$ (Hz), the horizontal geoelectric field  
 629 is given by (Equation (13))

$$631 \quad \mathbf{E} \equiv \begin{pmatrix} E_N \\ E_E \end{pmatrix} = \frac{1}{i2\pi f} \mathbf{Z} \begin{pmatrix} \frac{dB_N}{dt} \\ \frac{dB_E}{dt} \end{pmatrix} \quad (A.2)$$

632 Substituting (A.1) into (A.2) gives

$$634 \quad \begin{pmatrix} E_N \\ E_E \end{pmatrix} = \frac{1}{i2\pi f} \sqrt{\frac{2\pi f \mu_0}{\sigma}} e^{i\pi/4} \begin{pmatrix} 0 & 1 \\ -1 & 0 \end{pmatrix} \begin{pmatrix} \frac{dB_N}{dt} \\ \frac{dB_E}{dt} \end{pmatrix}$$

$$635 \quad = \sqrt{\frac{\mu_0}{2\pi f \sigma}} e^{-i\pi/4} \begin{pmatrix} \frac{dB_E}{dt} \\ -\frac{dB_N}{dt} \end{pmatrix}$$

636  
 637 By comparing components it is observed that  $|E_N| \propto |dB_E/dt|$  (where  $\propto$  denotes proportionality) and  $|E_E| \propto$   
 638  $|dB_N/dt|$ , and so  $|E| = \sqrt{E_N^2 + E_E^2} \propto R_n$ , where  $R_n$  is defined using the expression in Equation (2). Approximate

640 proportionality may be observed when the impedance  $\mathbf{Z}$  differs only slightly from the half-space model of  
641 impedance in (A.1).  
642

IAGA code	Location	Geodetic latitude (°N)	Geodetic longitude (°E)	Mean Corrected Geomagnetic latitude (°N)	Mean Corrected Geomagnetic longitude (°E)
ABG	Alibag, India	18.62	72.87	12.19	145.59
ABK	Abisko, Sweden	68.35	18.82	65.29	101.98
AMS	Martin-de-Viviès, Amsterdam I.	-37.8	77.57	-49.10	138.76
AND	Andenes, Norway	69.3	16.03	66.53	99.89
API	Apia, Samoa	-13.8	188.22	-15.59	-97.20
ASC	Ascension Island	-7.95	345.62	-10.37	56.47
ASP	Alice Springs, Australia	-23.77	133.88	-34.06	-152.63
ATU	Attu, India	67.93	306.43	74.19	38.37
BDV	Budkov, Czechia	49.07	14.02	44.40	89.37
BEL	Belsk, Poland	51.83	20.8	47.55	96.06
BFE	Brorfelde, Denmark	55.62	11.67	52.03	89.51
BJN	Bjørnøya, Svalbard	74.5	19.2	71.47	107.94
BLC	Baker Lake, Canada	64.33	263.97	74.01	-32.85
BMT	Beijing Ming Tombs, China	40.3	116.2	34.81	-170.72
BOU	Boulder, USA	40.13	254.77	49.04	-40.52
BRW	Utqiagvik, Alaska, USA	71.3	203.25	69.95	-109.37
BSL	Bay St Louis, USA	30.35	270.37	41.23	-19.39
CBB	Cambridge Bay, Canada	69.1	255	77.32	-51.99
CBI	Chichi-jima, Japan	27.15	142.3	19.83	-146.53
CDC	Cape Dorset, Canada	64.2	283.4	73.54	2.26
CHD	Chokurdakh, Russia	70.62	147.89	65.11	-146.75
CLF	Chambon-la-forêt, France	48.02	2.27	43.42	79.46
CMO	College, Alaska, USA	64.87	212.14	64.99	-96.46
CNB	Canberra, Australia	-34.1	150.7	-43.93	-131.74
CSY	Casey, Antarctica	-66.28	110.53	-80.79	156.40
CTA	Charters Towers, Australia	-20.1	146.3	-29.15	-139.40
CZT	Port-Alfred, Crozet Is.	-46.43	51.87	-53.25	106.05
DAW	Dawson City, Canada	64.05	220.89	65.94	-86.42
DLR	Del Rio, USA	29.49	259.08	38.87	-34.04
DMH	Danmarkshavn, Greenland	76.77	341.37	77.15	85.12
DOU	Dourbes, Belgium	50.1	4.6	45.79	81.68
DRV	Dumont d'Urville, Antarctica	-66.67	140.01	-80.65	-124.47
DRW	Darwin, Australia	-12.4	130.9	-21.53	-156.74
<b>ESK</b>	<b>Eskdalemuir, Scotland, UK</b>	<b>55.32</b>	<b>356.8</b>	<b>52.65</b>	<b>77.41</b>
EWA	Ewa Beach, Hawaii, USA	21.32	202	21.43	-90.00
EYR	Eyrewell, New Zealand	-43.4	172.4	-50.13	-103.35
FCC	Fort Churchill, Canada	58.76	265.92	69.04	-28.23
FHB	Paamiut, Greenland	62	310.32	67.63	39.03
FMC	Fort McMurray, Canada	56.66	248.79	64.29	-51.11
FRD	Fredericksburg, USA	38.2	282.63	49.08	-2.14
FRN	Fresno, USA	37.1	240.3	43.05	-56.30
FSP	Fort Simpson, Canada	61.76	238.77	67.34	-66.07
FUR	Fürstfeldbruck, Germany	48.17	11.28	43.33	86.85
FYU	Fort Yukon, Canada	66.57	214.7	67.28	-93.86
GDH	Qeqertarsuaq, Greenland	69.25	306.47	75.79	40.39
GHB	Nuuk, Greenland	64.17	308.27	70.18	37.83
GIM	Gillam, Canada	56.38	265.36	66.24	-27.15
GLN	Glenlea, Canada	49.65	262.88	60.06	-31.75
GNA	Gnangara, Australia	-31.8	116	-43.98	-172.78
GUA	Guam	13.59	144.87	5.96	-144.13
GUI	Güfmar, Canary Is.	28.32	343.57	12.91	60.66
<b>HAD</b>	<b>Hartland, England, UK</b>	<b>50.98</b>	<b>355.52</b>	<b>47.55</b>	<b>74.87</b>
HBK	Hartebeesthoek, S. Africa	-25.88	27.71	-36.09	94.69
HER	Hermanus, S. Africa	-34.43	19.23	-42.31	82.28
HLP	Hel, Poland	54.61	18.82	50.74	94.98
HON	Honolulu, Hawaii, USA	21.32	202	21.50	-90.13
HRB	Hurbanovo, Slovakia	47.86	18.19	43.03	92.69
HRN	Hornsund, Svalbard	77	15.6	74.18	108.69
HTY	Hatizyo, Japan	33.12	139.8	25.90	-148.91
IQA	Iqaluit, Canada	63.75	291.48	72.32	15.00
IRT	Irkoutsk, Russia	52.17	104.45	47.58	177.74
KAG	Kagoshima, Japan	31.48	130.72	24.80	-157.02
KAK	Kakioka, Japan	36.23	140.18	29.13	-148.35
KDU	Kakadu, Australia	-12.69	132.47	-21.78	-155.03
KNY	Kanoya, Japan	31.42	130.88	24.64	-157.04
KUV	Kullorsuaq, Greenland	74.57	302.82	80.81	42.87
<b>LER</b>	<b>Lerwick, Scotland, UK</b>	<b>60.13</b>	<b>358.82</b>	<b>57.97</b>	<b>81.13</b>
LOV	Lovoe, Sweden	59.35	17.83	55.85	96.36
LRM	Learmonth, Australia	-22.22	114.1	-33.09	-174.14

LRV	Leirvogur, Iceland	64.18	338.3	65.02	67.19
LYR	Longyearbyen, Svalbard	78.2	15.83	75.34	110.77
MAB	Manhay, Belgium	50.3	5.68	46.00	82.63
MAW	Mawson Station, Antarctica	-67.61	62.88	-70.35	90.48
MCM	McMurdo Station, Antarctica	-77.85	166.67	-79.91	-31.86
MCQ	Macquarie Island	-54.5	158.95	-64.34	-111.60
MEA	Meanook, Canada	54.62	246.65	62.12	-54.58
MGD	Magadan, Russia	59.97	150.86	53.89	-140.23
MMB	Memambetsu, Japan	43.91	144.19	37.04	-144.39
MSR	Moshiri, Japan	44.37	142.27	37.65	-145.93
MUT	Muntinlupa, Philippines	14.37	121.02	6.87	-167.21
NAL	Ny Ålesund, Svalbard	78.92	11.95	76.27	109.73
NAQ	Narsarsuaq, Greenland	61.16	314.56	66.20	43.47
NCK	Nagyecenk, Hungary	47.63	16.72	42.72	91.38
NEW	Newport, USA	48.27	242.88	54.94	-56.65
NGK	Niemegk, Germany	52.07	12.68	47.94	89.00
NUR	Nurmijärvi, Finland	60.5	24.65	56.96	102.10
ONW	Onagawa, Japan	38.43	141.47	31.52	-146.75
OTT	Ottawa, Canada	45.4	284.45	56.13	0.83
PAF	Port-aux-Français, Kerguelen Is	-49.35	70.26	-58.51	122.00
PBQ	Poste-de-la-Baleine, Canada	55.28	282.26	66.00	-1.68
PGC	Pangnirtung, Canada	66.1	294.2	74.14	20.10
PHU	Phú Thủy, Vietnam	21.03	105.95	14.31	178.11
PIN	Pinawa, Canada	50.2	263.96	60.15	-28.46
PPT	Pamatai, Tahiti	-17.57	210.42	-16.52	-74.68
PST	Port Stanley, Falkland Is	-51.7	302.11	-38.48	10.59
RAL	Rabbit Lake, Canada	58.22	256.32	67.01	-41.19
RAN	Rankine Inlet, Canada	62.82	267.89	72.47	-24.22
RES	Resolute Bay, Canada	74.69	265.11	83.38	-41.05
SBA	Scott Base, Antarctica	-77.85	166.78	-79.90	-31.99
SCO	Ittoqqortoormiit, Greenland	70.48	338.03	71.50	72.09
SIT	Sitka, Alaska, USA	57.07	224.67	59.76	-80.12
SJG	San Juan, Puerto Rico	18.11	293.85	28.09	10.31
SKT	Maniitsoq, Greenland	65.42	307.1	71.59	37.19
SMI	Fort Smith, Canada	60.02	248.05	67.43	-53.48
SOD	Sodankylä, Finland	67.37	26.63	63.90	107.45
SOR	Sørøya, Norway	70.54	22.22	67.46	105.71
SPA	South Pole Station, Antarctica	-90	-	-73.95	18.61
SPT	San Pablo Toledo, Spain	39.55	355.65	32.08	71.89
STF	Kangerlussuaq, Greenland	67.02	309.28	72.76	40.95
STJ	St Johns, Canada	47.6	307.32	53.87	31.30
SVS	Savissivik, Greenland	76.02	294.9	83.22	34.23
TAL	Taloyoak, Canada	69.54	266.45	78.56	-29.33
THL	Qaanaaq, Greenland	77.47	290.77	85.33	33.59
THY	Tihany, Hungary	46.9	17.54	41.86	91.97
TIK	Tixie, Russia	71.58	129	66.15	-162.08
TRO	Tromsø, Norway	69.66	18.94	66.69	102.68
TRW	Trelew, Argentina	-43.25	294.68	-29.91	4.99
TSU	Tsumeb, Namibia	-19.22	17.7	-30.14	87.12
TUC	Tucson, USA	32.17	249.27	39.77	-45.36
UMQ	Uummannaq, Greenland	70.68	307.87	76.46	42.84
UPN	Upernavik, Greenland	72.78	303.85	79.03	40.68
VAL	Valentia, Ireland	51.93	349.75	49.19	70.39
VIC	Victoria, Canada	48.52	236.58	53.85	-64.08
WNG	Wingst, Germany	53.75	9.07	50.00	86.77
YKC	Yellowknife, Canada	62.48	245.52	69.50	-59.40

643 Table 1. Locations of the 125 magnetometer sites. Mean CG latitudes and longitudes are averages over all years for which 1-  
644 min cadence data was available at that site, computed using the International Geomagnetic Reference Field (IGRF) model.  
645 Sites in bold provided 1-s resolution data for this study.

## 646 Data Availability Statement

647 The 1-minute cadence magnetometer data used in this paper are available from <https://supermag.jhuapl.edu> and  
648 described in (Gjerloev, 2012). 1-second cadence UK magnetometer data are available from the British Geological  
649 Survey: [http://www.geomag.bgs.ac.uk/data\\_service/data/home.html](http://www.geomag.bgs.ac.uk/data_service/data/home.html). The electric field data used to calculate the

650 MT transfer functions are available within the ESA Space Weather framework: <https://swe.ssa.esa.int/BGS->  
 651 [federated](https://swe.ssa.esa.int/BGS-federated).

## 652 Acknowledgements

653 This work was funded by the UK Natural Environment Research Council (NERC) under grants NE/P016715/1 and NE/P017231/1 as part of  
 654 the UK “Space Weather Impacts on Ground-based Systems” (SWIGS) project. Magnetometer data were provided by SuperMAG (available  
 655 from <https://supermag.jhuapl.edu>) and we gratefully acknowledge contributions from the SuperMAG collaborators: Intermagnet; USGS, J. J.  
 656 Love; CARISMA, PI I. Mann; CANMOS; The S-RAMP Database, PI K. Yumoto and Dr K. Shiokawa; The SPIDR database; AARI, PI Oleg  
 657 Troshichev; The MACCS program, PI M. Engebretson, Geomagnetism Unit of the Geological Survey of Canada; GIMA; MEASURE, UCLA  
 658 IGPP and Florida Institute of Technology; SAMBA, PI E. Zesta; 210 Chain, PI K. Yumoto; SAMNET, PI F. Honary; The IMAGE  
 659 magnetometer network, PI L. Juusola; AUTUMN, PI M. Connors; DTU Space, PI A. Willer; South Pole and McMurdo Magnetometer, PI’s  
 660 L.J. Lanzarotti and A. T. Weatherwax; ICESTAR; RAPIDMAG; British Antarctic Survey; MacMac, PI Dr P. Chi; BGS, PI Dr S. Macmillan;  
 661 Pushkov Institute of Terrestrial Magnetism, Ionosphere and Radio Wave Propagation (IZMIRAN); GFZ, PI Dr J. Matzka; MFGI, PI B. Heilig;  
 662 IGFPAS, PI J. Reda; University of L’Aquila, PI M. Vellante; BCMT, V. Lesur and A. Chambodut; Data obtained in cooperation with  
 663 Geoscience Australia, PI M. Costelloe; AALPIP, co-PIs B. Clauer and M. Hartinger; SuperMAG, PI J. W. Gjerloev; Sodankylä Geophysical  
 664 Observatory, PI T. Raita; Polar Geophysical Institute, A. Yahnin and Y. Sakharov; Geological Survey of Sweden, G. Schwartz; Swedish  
 665 Institute of Space Physics, M. Yamauchi; UiT the Arctic University of Norway, M. G. Johnsen; Finnish Meteorological Institute, PI K.  
 666 Kauristie.  
 667

## 668 References

- 669  
 670 Adebessin, B. O., Pulkkinen, A., & Ngwira, C. M. (2016). The interplanetary and magnetospheric causes of extreme dB/dt at equatorial  
 671 locations. *Geophysical Research Letters*, 43(22), 11,501-11,509. <https://doi.org/10.1002/2016GL071526>  
 672 Akasofu, S.-I. (2017). Auroral Substorms: Search for Processes Causing the Expansion Phase in Terms of the Electric Current Approach.  
 673 *Space Science Reviews*, 212, 341–381. <https://doi.org/10.1007/s11214-017-0363-7>  
 674 Angelopoulos, V., Baumjohann, W., Kennel, C. F., Coroniti, F. V., Kivelson, M. G., Pellat, R., et al. (1992). Bursty bulk flows in the inner  
 675 central plasma sheet. *Journal of Geophysical Research*, 97, 4027–4039. <https://doi.org/10.1029/91JA02701>  
 676 Apatenkov, S. V., Pilipenko, V. A., Gordeev, E. I., Viljanen, A., Juusola, L., Belakhovsky, V. B., Sakharov, Y. A., & Selivanov, V. N. (2020).  
 677 Auroral Omega Bands are a Significant Cause of Large Geomagnetically Induced Currents. *Geophysical Research Letters*, 47,  
 678 e2019GL086677. <https://doi.org/10.1029/2019GL086677>  
 679 Baker, G. J., Donovan, E. F., & Jackel, B. J. (2003). A comprehensive survey of auroral latitude Pc5 pulsation characteristics. *Journal of*  
 680 *Geophysical Research: Space Physics*, 108(A10), 1–14. <https://doi.org/10.1029/2002JA009801>  
 681 Barnes, P. R., Rizy, D. T., McConnell, B. W., Tesche, F. M., & Taylor E. R. Jr. (1991). Electric Utility Industry Experience with Geomagnetic  
 682 Disturbances, ORNL–6665, 1–78, Oak Ridge National Lab., TN, USA. <https://doi.org/10.2172/10108452>  
 683 Beamish, D., Clark, T. D. G., Clarke, E., & Thomson, A. W. P. (2002). Geomagnetically induced currents in the UK: Geomagnetic variations  
 684 and surface electric fields. *Journal of Atmospheric and Solar-Terrestrial Physics*, 64(16), 1779–1792. [https://doi.org/10.1016/S1364-](https://doi.org/10.1016/S1364-6826(02)00127-X)  
 685 [6826\(02\)00127-X](https://doi.org/10.1016/S1364-6826(02)00127-X)  
 686 Bedrosian, P. A., & Love, J. J. (2015). Mapping geoelectric fields during magnetic storms: Synthetic analysis of empirical United States  
 687 impedances. *Geophysical Research Letters*, 42, 10160–10170. <https://doi.org/10.1002/2015GL066636>  
 688 Beggan, C. D. (2015). Sensitivity of geomagnetically induced currents to varying auroral electrojet and conductivity models. *Earth, Planets*  
 689 *and Space*, 67(1). <https://doi.org/10.1186/s40623-014-0168-9>  
 690 Beggan, C. D., Beamish, D., Richards, A., Kelly, G. S., & Alan, A. W. (2013). Prediction of extreme geomagnetically induced currents in the  
 691 UK high-voltage network. *Space Weather*, 11(7), 407–419. <https://doi.org/10.1002/swe.20065>  
 692 Beggan, C.D., Richardson, G.S., Baillie, O., Hübert, J., Thomson, A.W.P. (2021). Geoelectric field measurement, modelling and validation  
 693 during geomagnetic storms in the UK. *Journal of Space Weather and Space Climate*, 11. <https://doi.org/10.1051/swsc/2021022>

- 694 Belakhovsky, V., Pilipenko, V., Engebretson, M., Sakharov, Y., & Selivanov, V. (2019). Impulsive disturbances of the geomagnetic field as  
695 a cause of induced currents of electric power lines. *Journal of Space Weather and Space Climate*, 9, A18.  
696 <https://doi.org/10.1051/swsc/2019015>
- 697 Boteler, D. H. (2000). Geomagnetic effects on the pipe-to-soil potentials of a continental pipeline. *Advances in Space Research*, 26(1), 15–  
698 20. [https://doi.org/10.1016/s0273-1177\(99\)01020-0](https://doi.org/10.1016/s0273-1177(99)01020-0)
- 699 Boteler, D. H. (2021). Modeling Geomagnetic Interference on Railway Signaling Track Circuits. *Space Weather*, 19(1).  
700 <https://doi.org/10.1029/2020SW002609>
- 701 Boteler, D. H., & Pirjola, R. J. (2017). Modeling geomagnetically induced currents. *Space Weather*, 15(1), 258–276.  
702 <https://doi.org/10.1002/2016SW001499>
- 703 Buzulukova, N. (Ed.) (2017). *Extreme Events in Geospace: Origins, Predictability, and Consequences*. Elsevier. ISBN 9780128127018.
- 704 Cagniard, L. (1953). Basic Theory of the magneto-telluric method of geophysical prospecting. *Geophysics*, 18, 605–635.  
705 <https://doi.org/10.1190/1.1437915>
- 706 Cannon, P., Angling, M., Barclay, L., Curry, C., Dyer, C., Edwards, R., et al. (2013). *Extreme space weather: impacts on engineered systems  
707 and infrastructure*. Royal Academy of Engineering. Royal Academy of Engineering, London, U.K. ISBN 1-903496-95-0.  
708 <http://www.raeng.org.uk/spaceweather>
- 709 Carrington, R. C. (1859). Description of a Singular Appearance seen in the Sun on September 1, 1859. *Monthly Notices of the Royal  
710 Astronomical Society*, 20, 13–15. <https://doi.org/10.1093/mnras/20.1.13>
- 711 Carter, B. A., Yizengaw, E., Pradipta, R., Halford, A. J., Norman, R., & Zhang, K. (2015). Interplanetary shocks and the resulting  
712 geomagnetically induced currents at the equator. *Geophysical Research Letters*, 42(16), 6554–6559.  
713 <https://doi.org/10.1002/2015GL065060>
- 714 Chave, A. D., & Jones, A. G. (2012). *The magnetotelluric method*. Cambridge University Press. <https://doi.org/10.1017/CBO9781139020138>
- 715 Cliver, E. W., & Dietrich, W. F. (2013). The 1859 space weather event revisited: Limits of extreme activity. *Journal of Space Weather and  
716 Space Climate*, 3, 1–15. <https://doi.org/10.1051/swsc/2013053>
- 717 Coles, S., (2001). *An introduction to statistical modeling of extreme values*. Springer-Verlag Ltd, London, ISBN 978-1852334598.
- 718 Crooker, N. U. (1992). Reverse convection. *Journal of Geophysical Research*, 97(A12), 19363. <https://doi.org/10.1029/92ja01532>
- 719 Danskin, D. W., & Lotz, S. I. (2015). Analysis of geomagnetic hourly ranges. *Space Weather*, 13(8), 458–468.  
720 <https://doi.org/10.1002/2015SW001184>
- 721 Dimmock, A. P., Rosenqvist, L., Hall, J.-O., Viljanen, A., Yordanova, E., Honkonen, I., et al. (2019). The GIC and geomagnetic response  
722 over Fennoscandia to the 7–8 September 2017 geomagnetic storm. *Space Weather*, 17, 989–1010.  
723 <https://doi.org/10.1029/2018SW002132>
- 724 Engebretson, M., Glassmeier, K.-H., Stellmacher, M., Hughes, W. J., & Lühr, H. (1998). The dependence of high-latitude Pc5 wave power  
725 on solar wind velocity and on the phase of high-speed solar wind streams. *Journal of Geophysical Research: Space Physics*, 103(A11),  
726 26271–26283. <https://doi.org/10.1029/97ja03143>
- 727 Engebretson, M. J., Yeoman, T. K., Oksavik, K., Søråas, F., Sigernes, F., Moen, J. I., et al. (2013). Multi-instrument observations from  
728 Svalbard of a traveling convection vortex, electromagnetic ion cyclotron wave burst, and proton precipitation associated with a bow  
729 shock instability. *Journal of Geophysical Research: Space Physics*, 118, 2975–2997. <https://doi.org/10.1002/jgra.50291>
- 730 Engebretson, M. J., Pilipenko, V. A., Ahmed, L. Y., Posch, J. L., Steinmetz, E. S., Moldwin, M. B., et al. (2019a). Nighttime magnetic  
731 perturbation events observed in Arctic Canada: 1. Survey and statistical analysis. *Journal of Geophysical Research: Space Physics*,  
732 124, 7442–7458. <https://doi.org/10.1029/2019JA026794>
- 733 Engebretson, M. J., Steinmetz, E. S., Posch, J. L., Pilipenko, V. A., Moldwin, M. B., Connors, M. G., et al. (2019b). Nighttime magnetic  
734 perturbation events observed in Arctic Canada: 2. Multiple-instrument observations. *Journal of Geophysical Research: Space Physics*,  
735 124, 7459–7476. <https://doi.org/10.1029/2019JA026797>
- 736 Engebretson, M. J., Kirkeveld, K. R., Steinmetz, E. S., Pilipenko, V. A., Moldwin, M. B., & McCuen, B. A., et al. (2020). Interhemispheric  
737 comparisons of large nighttime magnetic perturbation events relevant to GICs. *Journal of Geophysical Research: Space Physics*, 125,  
738 e2020JA028128. <https://doi.org/10.1029/2020JA028128>
- 739 Engebretson, M. J., Pilipenko, V. A., Steinmetz, E. S., Moldwin, M. B., Connors, M. G., Boteler, D. H., et al. (2021). Nighttime magnetic  
740 perturbation events observed in Arctic Canada: 3. Occurrence and amplitude as functions of magnetic latitude, local time, and magnetic  
741 disturbance indices. *Space Weather*, 19, e2020SW002526. <https://doi.org/10.1029/2020SW002526>

- 742 Erinmez, I. A., Kappenman, J. G., & Radasky, W. A. (2002). Management of the geomagnetically induced current risks on the national grid  
 743 company's electric power transmission system. *Journal of Atmospheric and Solar-Terrestrial Physics*, 64(5–6), 743–756.  
 744 [https://doi.org/10.1016/S1364-6826\(02\)00036-6](https://doi.org/10.1016/S1364-6826(02)00036-6)
- 745 Eroshenko, E. A., Belov, A. V., Boteler, D., Gaidash, S. P., Lobkov, S. L., Pirjola, R., & Trichtchenko, L. (2010). Effects of strong geomagnetic  
 746 storms on Northern railways in Russia. *Advances in Space Research*, 46(9), 1102–1110. <https://doi.org/10.1016/j.asr.2010.05.017>
- 747 Falayi, E. O., Ogunmodimu, O., Bolaji, O. S., Ayanda, J. D., & Ojoniyi, O. S. (2017). Investigation of geomagnetic induced current at high  
 748 latitude during the storm-time variation. *NRIAG Journal of Astronomy and Geophysics*, 6(1), 131–140.  
 749 <https://doi.org/10.1016/j.nrjag.2017.04.010>
- 750 Faraday, M. (1832). Experimental researches in electricity. *Philosophical Transactions of the Royal Society*, 122, 125–161.  
 751 <https://doi.org/10.1098/rstl.1832.0006>
- 752 Fiori, R. A. D., Boteler, D. H., & Gillies, D. M. (2014). Assessment of GIC risk due to geomagnetic sudden commencements and identification  
 753 of the current systems responsible. *Space Weather*, 12, 76–91. <https://doi.org/10.1002/2013SW000967>
- 754 Freeman, M. P., Forsyth, C., & Rae, I. J. (2019). The Influence of Substorms on Extreme Rates of Change of the Surface Horizontal Magnetic  
 755 Field in the United Kingdom. *Space Weather*, 17(6), 827–844. <https://doi.org/10.1029/2018SW002148>
- 756 Friis-Christensen, E., McHenry, M. A., Clauer, C. R., & Vennerstrøm, S. (1988). Ionospheric traveling convection vortices observed near  
 757 the polar cleft: A triggered response to sudden changes in the solar wind. *Geophysical Research Letters*, 15(3), 253–256.  
 758 <https://doi.org/10.1029/GL015i003p00253>
- 759 Gaunt, C. T. (2016). Why space weather is relevant to electrical power systems. *Space Weather*, 14(1), 2–9.  
 760 <https://doi.org/10.1002/2015SW001306>
- 761 Gilleland, E. & Katz, R.W. (2016). extRemes 2.0: An extreme value analysis package in R. *Journal of Statistical Software*, 72(8), 1-39.  
 762 <https://doi.org/10.18637/jss.v072.i08>
- 763 Girgis, R., & Vedante, K. (2012). Effects of GIC on power transformers and power systems. *44th International Conference on Large High  
 764 Voltage Electric Systems (PES T&D), 7-10 May 2012, Orlando, FL, USA*, 1–8. <https://doi.org/10.1109/TDC.2012.6281595>
- 765 Gjerloev, J. W. (2011) A global ground-based magnetometer initiative, *Eos* 90, 230–231. <https://doi.org/10.1029/2009EO270002>
- 766 Gjerloev, J. W. (2012). The SuperMAG data processing technique. *Journal of Geophysical Research: Space Physics*, 117(9), 1–19.  
 767 <https://doi.org/10.1029/2012JA017683>
- 768 Hao, Y. X., Zong, Q. G., Zhou, X. Z., Rankin, R., Chen, X. R., Liu, Y., Fu, S. Y., Baker, D. N., Spence, H. E., Blake, J. B., Reeves, G. D., &  
 769 Claudepierre, S. G. (2019). Global-Scale ULF Waves Associated With SSC Accelerate Magnetospheric Ultrarelativistic Electrons.  
 770 *Journal of Geophysical Research: Space Physics*, 124, 1525–1538. <https://doi.org/10.1029/2018JA026134>
- 771 Hapgood, M., Angling, M. J., Attrill, G., Bisi, M., Cannon, P. S., Dyer, C., et al. (2021). Development of Space Weather Reasonable Worst  
 772 Case Scenarios for the UK National Risk Assessment. *Space Weather*, 19, e2020SW002593. <https://doi.org/10.1029/2020SW002593>
- 773 Hartinger, M. D., Shi, X., Lucas, G. M., Murphy, B. S., Kelbert, A., Baker, J. B. H., Rigler, E. J., & Bedrosian, P. A. (2020). Simultaneous  
 774 Observations of Geoelectric and Geomagnetic Fields Produced by Magnetospheric ULF Waves. *Geophysical Research Letters*, 47,  
 775 e2020GL089441. <https://doi.org/10.1029/2020GL089441>
- 776 Heyns, M. J., Lotz, S. I., & Gaunt, C. T. (2020). Geomagnetic Pulsations Driving Geomagnetically Induced Currents. *Space Weather*, 19,  
 777 e2020SW002557. <https://doi.org/10.1029/2020sw002557>
- 778 Hüser, R., & Wadsworth, J. L. (2020). Advances in statistical modeling of spatial extremes. *WIREs Computational Statistics*, 2020:e1537,  
 779 <https://doi.org/10.1002/wics.1537>
- 780 Ieda, A., Kauristie, K., Nishimura, Y., Miyashita, Y., Frey, H. U., Juusola, L., et al. (2018). Simultaneous observation of auroral substorm  
 781 onset in Polar satellite global images and ground-based all-sky images. *Earth, Planets and Space*, 70(1). <https://doi.org/10.1186/s40623-018-0843-3>
- 782
- 783 IEEE (2015) IEEE Guide for Establishing Power Transformer Capability while under Geomagnetic Disturbances, IEEE Std C57.163 2015,  
 784 3 September 2015, The Institute of Electrical and Electronics Engineers, Inc., ISBN 978-0-7381-9897-2.
- 785 Jankee, P., Chisepo, H., Adebayo, V., Oyedokun, D., & Gaunt, C. T. (2020). Transformer models and meters in MATLAB and PSCAD for  
 786 GIC and leakage dc studies. 2020 International SAUPEC/RobMech/PRASA Conference, SAUPEC/RobMech/PRASA 2020.  
 787 <https://doi.org/10.1109/SAUPEC/RobMech/PRASA48453.2020.9041060>
- 788 Jorgensen, A. M., Spence, H. E., Hughes, T. J., & McDiarmid, D. (1999). A study of omega bands and Ps6 pulsations on the ground, at low  
 789 altitude and at geostationary orbit. *Journal of Geophysical Research: Space Physics*, 104(A7), 14705–14715.  
 790 <https://doi.org/10.1029/1998ja900100>

- 791 Kappenman, J. G. (2003). Storm sudden commencement events and the associated geomagnetically induced current risks to ground-based  
 792 systems at low-latitude and midlatitude locations. *Space Weather*, 1(3), 1016. <https://doi.org/10.1029/2003sw000009>
- 793 Kappenman, J. G. (2004). The evolving vulnerability of electric power grids, *Space Weather*, 2, S01004.  
 794 <https://doi.org/10.1029/2003SW000028>.
- 795 Kataoka, R., Fukunishi, H., & Lanzerotti, L. J. (2003). Statistical identification of solar wind origins of magnetic impulse events. *Journal of*  
 796 *Geophysical Research: Space Physics*, 108(A12). <https://doi.org/10.1029/2003JA010202>
- 797 Kelbert, A., Egbert, G.D., & Schultz, A. (2011). IRIS DMC Data Services Products: EMTF, The Magnetotelluric Transfer Functions,  
 798 <https://doi.org/10.17611/DP/EMTF.1>.
- 799 Kelbert, A., Balch, C. C., Pulkkinen, A., Egbert, G. D., Love, J. J., Rigler, E. J., & Fujii, I. (2017). Methodology for time-domain estimation  
 800 of storm time geoelectric fields using the 3-D magnetotelluric response tensors. *Space Weather*, 15(7), 874–894.  
 801 <https://doi.org/10.1002/2017SW001594>
- 802 Kelbert, A., Erofeeva, S., Trabant, C., Karstens, R., & Van Fossen, M. (2018). Taking magnetotelluric data out of the drawer, *Eos*, 99,  
 803 <https://doi.org/10.1029/2018EO112859>
- 804 Knipp, D. J. (2011). Understanding space weather and the physics behind it (M. McQuade & D. Kirkpatrick (eds.)). McGraw-Hill Companies,  
 805 Inc., ISBN 978-0-07-340890-3.
- 806 Kozyreva, O. V., Pilipenko, V. A., Belakhovsky, V. B., & Sakharov, Y.A.. (2018). Ground geomagnetic field and GIC response to March  
 807 17, 2015, storm. *Earth, Planets and Space*, 70, 157. <https://doi.org/10.1186/s40623-018-0933-2>
- 808 Lanzerotti, L. J., Konik, R. M., Wolfe, A., Venkatesan, D., & MacLennan, C. G. (1991). Cusp latitude magnetic impulse events: 1. Occurrence  
 809 statistics. *Journal of Geophysical Research: Space Physics*, 96(A8), 14009–14022. <https://doi.org/10.1029/91ja00567>
- 810 Laundal, K. M., & Richmond, A. D. (2017). Magnetic coordinate systems. *Space Science Reviews*, 206, 27. [https://doi.org/10.1007/s11214-](https://doi.org/10.1007/s11214-016-0275-y)  
 811 [016-0275-y](https://doi.org/10.1007/s11214-016-0275-y)
- 812 Liu, J., Angelopoulos, V., Zhou, X.-Z., and Runov A. (2014). Magnetic flux transport by dipolarizing flux bundles, *Journal of Geophysical*  
 813 *Research: Space Physics*, 119, 909–926. <https://doi.org/10.1002/2013JA019395>
- 814 Love, J. J. and Chulliat, A. (2013), An international network of magnetic observatories, *Eos Transactions, American Geophysical Union*,  
 815 94(42), 373–374. <https://doi.org/10.1002/2013EO420001>
- 816 Love, J. J., Coisson, P., & Pulkkinen, A. (2016a). Global statistical maps of extreme-event magnetic observatory 1 min first differences in  
 817 horizontal intensity. *Geophysical Research Letters*, 43(9), 4126–4135. <https://doi.org/10.1002/2016GL068664>
- 818 Love, J. J., Pulkkinen, A., Bedrosian, P. A., Jonas, S., Kelbert, A., Rigler, E. J., et al. (2016). Geoelectric hazard maps for the continental  
 819 United States. *Geophysical Research Letters*, 43(18), 9415–9424. <https://doi.org/10.1002/2016GL070469>
- 820 McPherron, R. L. (2005). Magnetic pulsations: Their sources and relation to solar wind and geomagnetic activity. *Surveys in Geophysics*,  
 821 26(5), 545–592. <https://doi.org/10.1007/s10712-005-1758-7>
- 822 Milan, S. E., Clausen, L. B. N., Coxon, J. C., Carter, J. A., Walach, M.-T., Laundal, K., Østgaard, N., Tenfjord, P., Reistad, J., Snekvik, K.,  
 823 Korth, H., & Anderson, B. J. (2017). Overview of Solar Wind–Magnetosphere–Ionosphere–Atmosphere Coupling and the Generation  
 824 of Magnetospheric Currents. *Space Science Reviews*, 206(1–4), 547–573. <https://doi.org/10.1007/s11214-017-0333-0>
- 825 Milan, S. E., Carter, J. A., Bower, G. E., Imber, S. M., Paxton, L. J., Anderson, B. J., Hairston, M. R., & Hubert, B. (2020). Dual-Lobe  
 826 Reconnection and Horse-Collar Auroras. *Journal of Geophysical Research: Space Physics*, 125(10).  
 827 <https://doi.org/10.1029/2020JA028567>
- 828 Molinski, T. S. (2002). Why utilities respect geomagnetically induced currents. *Journal of Atmospheric and Solar-Terrestrial Physics*,  
 829 64(2002), 1765–1778. [https://doi.org/10.1016/S1364-6826\(02\)00126-8](https://doi.org/10.1016/S1364-6826(02)00126-8)
- 830 NERC (2017), Transformer thermal impact assessment: Project 2013-03 (Geomagnetic Disturbance Mitigation), North American Electricity  
 831 Reliability Corporation, pp. 1–16, Atlanta, GA. Available online:  
 832 [http://www.nerc.com/pa/Stand/Project201303GeomagneticDisturbanceMitigation/Thermal\\_Impact\\_Assessment\\_2017\\_October\\_Clea](http://www.nerc.com/pa/Stand/Project201303GeomagneticDisturbanceMitigation/Thermal_Impact_Assessment_2017_October_Clean.pdf)  
 833 [n.pdf](http://www.nerc.com/pa/Stand/Project201303GeomagneticDisturbanceMitigation/Thermal_Impact_Assessment_2017_October_Clean.pdf)
- 834 Nevanlinna, H., Tenhunen, P., Pirjola, R., Annanpalo, J., & Pulkkinen, A. (2001). Breakdown caused by a geomagnetically induced current  
 835 in the Finnish telesystem in 1958. *Journal of Atmospheric and Solar-Terrestrial Physics*, 63(10), 1099–1103.  
 836 [https://doi.org/10.1016/S1364-6826\(01\)00021-9](https://doi.org/10.1016/S1364-6826(01)00021-9)
- 837 Newell, P. T., & Gjerloev, J. W. (2011). Evaluation of SuperMAG auroral electrojet indices as indicators of substorms and auroral power.  
 838 *Journal of Geophysical Research*, 116, A12211. <https://doi.org/10.1029/2011JA016779>
- 839 Ngwira, C. M., Pulkkinen, A., Wilder, F. D., & Crowley, G. (2013). Extended study of extreme geoelectric field event scenarios for  
 840 geomagnetically induced current applications. *Space Weather*, 11, 121–131. <https://doi.org/10.1002/swe.20021>

- 841 Ngwira, C. M., Pulkkinen, A., Kuznetsova, M. M., and Glocer, A. (2014). Modeling extreme “Carrington-type” space weather events using  
 842 three-dimensional global MHD simulations, *Journal of Geophysical Research: Space Physics*, *119*, 4456–4474,  
 843 <https://doi.org/10.1002/2013JA019661>
- 844 Ngwira, C. M., Sibeck, D., Silveira, M. V. D., Georgiou, M., Weygand, J. M., Nishimura, Y., & Hampton, D. (2018). A study of intense  
 845 local dB/dt variations during two geomagnetic storms. *Space Weather*, *16*(6), 676–693. <https://doi.org/10.1029/2018SW001911>
- 846 Nikitina, L., Trichtchenko, L., & Boteler, D. H. (2016). Assessment of extreme values in geomagnetic and geoelectric field variations for  
 847 Canada. *Space Weather*, *14*(7), 481–494. <https://doi.org/10.1002/2016SW001386>
- 848 Oyedokun, D. T. O., & Cilliers, P. J. (2018). Geomagnetically induced currents: A threat to modern power systems. *Classical and Recent*  
 849 *Aspects of Power System Optimization* Ed.(s): A. F. Zobaa, S. H. E. Abdel Aleem, & A. Y. Abdelaziz. Academic Press. 421–462. ISBN  
 850 9780128124413. <https://doi.org/10.1016/B978-0-12-812441-3.00016-1>
- 851 Pahud, D. M., Rae, I. J., Mann, I. R., Murphy, K. R., & Amalraj, V. (2009). Ground-based Pc5 ULF wave power: Solar wind speed and MLT  
 852 dependence. *Journal of Atmospheric and Solar-Terrestrial Physics*, *71*(2009), 1082–1092. <https://doi.org/10.1016/j.jastp.2008.12.004>
- 853 Pilipenko, V., Kozyreva, O., Belakhovsky, V., Engebretson, M. J., & Samsonov, S. (2010). Generation of magnetic and particle Pc5 pulsations  
 854 during the recovery phase of strong magnetic storms. *Proceedings of the Royal Society A: Mathematical, Physical and Engineering*  
 855 *Sciences*, *466*(2123), 3363–3390. <https://doi.org/10.1098/rspa.2010.0079>
- 856 Pilipenko, V. A., Fedorov, E. N., Hartinger, M. D., & Engebretson, M. J. (2019). Electromagnetic fields of magnetospheric ULF disturbances  
 857 in the ionosphere: Current/voltage dichotomy. *Journal of Geophysical Research: Space Physics*, *124*, 109–121.  
 858 <https://doi.org/10.1029/2018JA026030>
- 859 Pirjola, R. (1984). Estimation of the electric field on the Earth’s surface during a geomagnetic variation, *Geophysica*, *20*(2), 89–103, ISSN  
 860 2324-0741
- 861 Pirjola, R. (2010). Derivation of characteristics of the relation between geomagnetic and geoelectric variation fields from the surface  
 862 impedance for a two-layer earth. *Earth, Planets and Space*, *62*(3), 287–295. <https://doi.org/10.5047/eps.2009.09.002>
- 863 Pothier, N. M., Weimer, D. R., & Moore, W. B. (2015). Quantitative maps of geomagnetic perturbation vectors during substorm onset and  
 864 recovery. *Journal of Geophysical Research: Space Physics*, *120*, 1197–1214. <https://doi.org/10.1002/2014JA020602>
- 865 Pulkkinen, A., & Kataoka, R. (2006). S-transform view of geomagnetically induced currents during geomagnetic superstorms. *Geophysical*  
 866 *Research Letters*, *33*(12), 3–6. <https://doi.org/10.1029/2006GL025822>
- 867 Pulkkinen, A., Viljanen, A., Pajunpää, K., & Pirjola, R. (2001). Recording and occurrence of geomagnetically induced currents in the Finnish  
 868 natural gas pipeline network. *Journal of Applied Geophysics*, *48*(4), 219–231. [https://doi.org/10.1016/S0926-9851\(01\)00108-2](https://doi.org/10.1016/S0926-9851(01)00108-2)
- 869 Pulkkinen, A., Viljanen, A., & Pirjola, R. (2006). Estimation of geomagnetically induced current levels from different input data. *Space*  
 870 *Weather*, *4*(8), S08005. <https://doi.org/10.1029/2006SW000229>
- 871 Pulkkinen, A., Kataoka, R., Watari, S., & Ichiki, M. (2010). Modeling geomagnetically induced currents in Hokkaido, Japan. *Advances in*  
 872 *Space Research*, *46*(9), 1087–1093. <https://doi.org/10.1016/j.asr.2010.05.024>
- 873 Pulkkinen, A., Bernabeu, E., Eichner, J., Beggan, C., & Thomson, A. W. P. (2012). Generation of 100-year geomagnetically induced current  
 874 scenarios. *Space Weather*, *10*, S04003. <https://doi.org/10.1029/2011SW000750>
- 875 Pulkkinen, A., Bernabeu, E., Thomson, A., Viljanen, A., Pirjola, R., Boteler, D., et al. (2017). Geomagnetically induced currents: Science,  
 876 engineering, and applications readiness. *Space Weather*, *15*, 828–856. <https://doi.org/10.1002/2016SW001501>
- 877 Rogers, N. C., Wild, J. A., Eastoe, E. F., Gjerloev, J. W., & Thomson, A. W. P. (2020). A global climatological model of extreme geomagnetic  
 878 field fluctuations. *Journal of Space Weather and Space Climate*, *10*, 5. <https://doi.org/10.1051/swsc/2020008>
- 879 Russell, C. T., & McPherron, R. L. (1973). Semiannual variation of geomagnetic activity. *Journal of Geophysical Research*, *78*(1), 92–108.  
 880 <https://doi.org/10.1029/ja078i001p00092>
- 881 Saito, T. (1978). Long-period irregular magnetic pulsation, Pi3. *Space Science Reviews*, *21*, 427–467. <https://doi.org/10.1007/BF00173068>
- 882 Shepherd, S. G. (2014). Altitude-adjusted corrected geomagnetic coordinates: Definition and functional approximations. *Journal of*  
 883 *Geophysical Research: Space Physics*, *119*(9), 7501–7521. <https://doi.org/10.1002/2014JA020264>
- 884 Simpson, F., & Bahr, K. (2005). Practical Magnetotellurics. Cambridge University Press. <https://doi.org/10.1017/CBO9780511614095>
- 885 Smirnov, M. Y. (2003). Magnetotelluric data processing with a robust statistical procedure having a high breakdown point. *Geophysical*  
 886 *Journal International*, *152*(1):1–7. <https://doi.org/10.1046/j.1365-246X.2003.01733.x>
- 887 Smith, A. W., Freeman, M. P., Rae, I. J., & Forsyth, C. (2019). The Influence of Sudden Commencements on the Rate of Change of the  
 888 Surface Horizontal Magnetic Field in the United Kingdom. *Space Weather*, *17*(11), 1605–1617.  
 889 <https://doi.org/10.1029/2019SW002281>
- 890 Thomson, A. W. P., & Flower, S. M. (2021). Modernizing a global magnetic partnership, *Eos*, *102*, <https://doi.org/10.1029/2021EO156569>

- 891 Thomson, A. W. P., Gaunt, C. T., Cilliers, P., Wild, J. A., Opperman, B., Mckinnell, L.-A., et al. (2010) Present day challenges in  
 892 understanding the geomagnetic hazard to national power grids. *Advances in Space Research*, 45(9), 1182–1190.  
 893 <https://doi.org/10.1016/j.asr.2009.11.023>
- 894 Thomson, A. W. P., Dawson, E. B., & Reay, S. J. (2011). Quantifying extreme behavior in geomagnetic activity. *Space Weather*, 9, S10001.  
 895 <https://doi.org/10.1029/2011SW000696>
- 896 Töth, G., Meng, X., Gombosi, T. I., & Rastätter, L. (2014). Predicting the time derivative of local magnetic perturbations. *Journal of*  
 897 *Geophysical Research: Space Physics*, 119(1), 310–321. <https://doi.org/10.1002/2013JA019456>
- 898 Trichtchenko, L., & Boteler, D. H. (2004). Modeling geomagnetically induced currents using geomagnetic indices and data. *IEEE*  
 899 *Transactions on Plasma Science*, 32(4), 1459–1467. <https://doi.org/10.1109/TPS.2004.830993>
- 900 Vennerström, S. (1999). Dayside magnetic ULF power at high latitudes: A possible long-term proxy for the solar wind velocity? *Journal of*  
 901 *Geophysical Research: Space Physics*, 104(A5), 10145–10157. <https://doi.org/10.1029/1999ja900015>
- 902 Viljanen, A. (1997). The relation between geomagnetic variations and their time derivatives and implications for estimation of induction risks.  
 903 *Geophysical Research Letters*, 24(6), 631–634. <https://doi.org/10.1029/97GL00538>
- 904 Viljanen, A., Nevanlinna, H., Pajunpää, K., & Pulkkinen, A. (2001). Time derivative of the horizontal geomagnetic field as an activity  
 905 indicator. *Annales Geophysicae*, 19(9), 1107–1118. <https://doi.org/10.5194/angeo-19-1107-2001>
- 906 Viljanen, A., Wintoft, P., & Wik, M. (2015). Regional estimation of geomagnetically induced currents based on the local magnetic or electric  
 907 field. *Journal of Space Weather and Space Climate*, 5, A24. <https://doi.org/10.1051/swsc/2015022>
- 908 Wait, J. R., (1962). Theory of magneto-telluric fields. *Journal of Research of the National Bureau of Standards - D. Radio Propagation*.  
 909 66D(5), 509–541. <http://dx.doi.org/10.6028/jres.066D.052>
- 910 Wang, H., Ridley, A. J., & Lühr, H. (2008). SWMF simulation of field-aligned currents for a varying northward and duskward IMF with  
 911 nonzero dipole tilt. *Annales Geophysicae*, 26(6), 1461–1477. <https://doi.org/10.5194/angeo-26-1461-2008>
- 912 Watanabe, M., Kabin, K., Sofko, G. J., Rankin, R., Gombosi, T. I., Ridley, A. J., & Clauer, C. R. (2005). Internal reconnection for northward  
 913 interplanetary magnetic field. *Journal of Geophysical Research: Space Physics*, 110(A6), 1–18. <https://doi.org/10.1029/2004JA010832>
- 914 Watari, S., Kunitake, M., Kitamura, K., Hori, T., Kikuchi, T., Shiokawa, K., et al. (2009). Measurements of geomagnetically induced current  
 915 in a power grid in Hokkaido, Japan. *Space Weather*, 7(3). <https://doi.org/10.1029/2008SW000417>
- 916 Wei, D., Dunlop, M. W., Yang, J., Dong, X., Yu, Y., & Wang, T. (2021). Intense dB/dt variations driven by near-Earth Bursty Bulk Flows  
 917 (BBFs): A case study. *Geophysical Research Letters*. <https://doi.org/10.1029/2020GL091781>
- 918 Weigel, R. S., Vassiliadis, D., & Klimas, A. J., (2002) Coupling of the solar wind to temporal fluctuations in ground magnetic fields, *Geophys.*  
 919 *Res. Lett.*, 29(19), 1915, <https://doi.org/10.1029/2002GL014740>
- 920 Wik, M., Pirjola, R., Lundstedt, H., Viljanen, A., Wintoft, P., & Pulkkinen, A. (2009). Space weather events in July 1982 and October 2003  
 921 and the effects of geomagnetically induced currents on Swedish technical systems. *Annales Geophysicae*, 27(4), 1775–1787.  
 922 <https://doi.org/10.5194/angeo-27-1775-2009>
- 923 Wild, J. A., Yeoman, T. K., Eglitis, P., & Opgenoorth, H. J. (2000). Multi-instrument observations of the electric and magnetic field structure  
 924 of omega bands. *Annales Geophysicae*, 18(1), 99–110. <https://doi.org/10.1007/s00585-000-0099-6>
- 925 Wild, J. A., Woodfield, E. E., Donovan, E., Fear, R. C., Grocott, A., Lester, M., et al. (2011). Midnight sector observations of auroral omega  
 926 bands. *J. Geophys. Res.*, 116(A5), A00I30. <https://doi.org/10.1029/2010JA015874>
- 927 Winter, L. M., Gannon, J., Pernak, R., Huston, S., Quinn, R., Pope, E., et al. (2017), Spectral scaling technique to determine extreme  
 928 Carrington-level geomagnetically induced currents effects, *Space Weather*, 15, 713–725, <https://doi.org/10.1002/2016SW001586>
- 929 Wintoft, P. (2005). Study of the solar wind coupling to the time difference horizontal geomagnetic field. *Annales Geophysicae*, 23(5), 1949–  
 930 1957. <https://doi.org/10.5194/angeo-23-1949-2005>
- 931 Wintoft, P., Wik, M., Lundstedt, H., & Eliasson, L. (2005). Predictions of local ground geomagnetic field fluctuations during the 7-10  
 932 November 2004 events studied with solar wind driven models. *Annales Geophysicae*, 23(9), 3095–3101. <https://doi.org/10.5194/angeo-23-3095-2005>
- 933 Wintoft, P., Wik, M., & Viljanen, A. (2015). Solar wind driven empirical forecast models of the time derivative of the ground magnetic field.  
 934 *Journal of Space Weather and Space Climate*, 5(A7). <https://doi.org/10.1051/swsc/2015008>
- 935 Wintoft, P., Viljanen, A., & Wik, M. (2016). Extreme value analysis of the time derivative of the horizontal magnetic field and computed  
 936 electric field. *Annales Geophysicae*, 34, 485–491. <https://doi.org/10.5194/angeo-34-485-2016>
- 937 Zesta, E., Hughes, W. J., & Engebretson, M. J. (2002). A statistical study of traveling convection vortices using the Magnetometer Array for  
 938 Cusp and Cleft Studies. *Journal of Geophysical Research: Space Physics*, 107(A10), 1–21. <https://doi.org/10.1029/1999JA000386>
- 939

- 940 Zhang, X. Y. (2010). ULF waves excited by negative/positive solar wind dynamic pressure impulses at geosynchronous orbit. *Journal of*  
941 *Geophysical Research*, 115, A10221. <https://doi.org/10.1029/2009JA015016>
- 942 Zhao, H., & Zong, Q.-G. (2012). Seasonal and diurnal variation of geomagnetic activity: Russell-McPherron effect during different IMF  
943 polarity and/or extreme solar wind conditions. *Journal of Geophysical Research*, 117, A11222. <https://doi.org/10.1029/2012JA017845>
- 944 Ziesolleck, C. W. S., & McDiarmid, D. R. (1995). Statistical survey of auroral latitude Pc5 spectral and polarization characteristics. *Journal*  
945 *of Geophysical Research*, 100(A10), 19299. <https://doi.org/10.1029/95ja00434>